Microporous and Mesoporous Materials 405 (2026) 114080

Contents lists available at ScienceDirect

Microporous and Mesoporous Materials

journal homepage: www.elsevier.com/locate/micromeso

Mesoporous silica as a tunable support for dual-function Ba–Ru catalysts: impact on CO_2 adsorption and methanation performance

S. Molina-Ramirez [a], G. Nava [b], E. Finocchio [c,*], L. Lietti [b], L. Viganò [a], M. Di Virgilio [a], B. Di Credico [d], R. Scotti [d], C. Cristiani [a], L. Castoldi [b,**]

[a] Dipartimento di Chimica, Materiali e Ingegneria Chimica "Giulio Natta", Politecnico di Milano, Piazza Leonardo Da Vinci 32, Milano, Italy
[b] Dipartimento di Energia, Laboratory of Catalysis and Catalytic Processes, Politecnico di Milano, Via la Masa 34, Milano, Italy
[c] Dipartimento di Ingegneria Civile, Chimica e Ambientale, Università di Genova (UNIGE), Via all'Opera Pia 15, Genova, Italy
[d] Dipartimento di Scienza dei Materiali, Università Milano-Bicocca, Piazza dell'Ateneo Nuovo 1, Milano, Italy

ARTICLE INFO

Keywords:
Silica
FT-IR spectroscopy
DFM
CO_2 capture and utilization
Barium
Ruthenium

ABSTRACT

The integration of CO_2 capture and catalytic methanation into a single material platform presents an efficient route toward carbon-neutral fuel production. In this work, we investigate silica-supported dual-function materials (DFMs) comprising Ba as the CO_2 storage component and Ru as the methanation catalyst. A series of Ba-Ru/SiO_2 materials were synthesized via incipient wetness impregnation, with varying Ba loadings (16-32 wt%) and promoter deposition sequences. Structural, morphological, and surface analyses (BET, XRD, FT-IR) revealed the formation and thermal evolution of distinct carbonate species as a function of Ba content and preparation method. CO_2-TPD and H_2-TPSR experiments demonstrated that the impregnation order influences the nature, strength, and regenerability of the adsorbed carbonate species. Increasing Ba loading enhances CO_2 uptake and promotes the formation of thermally stable bridging carbonates, while Ru positioning affects methanation activity and carbonate reactivity. Compared to alumina-based DFMs, silica-supported systems exhibit distinct carbonate populations and lower-temperature regeneration behavior due to the non-interacting nature of the support. These findings offer new insights into the design of mesoporous DFMs with tunable CO_2 sorption and conversion performance, highlighting the properties of silica as support for integrated carbon capture and utilization.

1. Introduction

The rising concentration of atmospheric CO_2 [1], mainly caused by anthropogenic CO_2 emissions from the power generation and industry sectors [2], is producing serious environmental impacts. To mitigate this issue, two main strategies are typically considered: replacing fossil fuels with synthetic fuels produced using green H_2, and capturing CO_2 from the environment. In this context, CO_2 capture is expected to play a larger role because it can be integrated into already existing industrial processes, and is considered more cost-effective than switching entirely to green fuels, also given the limited availability of large amounts of renewable energy.

Several approaches for the mitigation of atmospheric CO_2 have been proposed, including the capture from point-source emissions or from the environment, also known as Direct Air Capture (DAC) [3]. Despite the difference in CO_2 level – respectively about 10-16% [4] vs 420 ppm] [5] - both imply the absorption of CO_2 utilizing liquid solvents, principally amines [6], or the adsorption of CO_2 utilizing solid sorbents, such as zeolites or metal oxides [7,8] which rely respectively on physisorption and chemisorption.

The captured CO_2 is then released through temperature or pressure swings, resulting in a concentrated CO_2 stream that can be injected under the ground (Carbon Capture and Storage, CCS) or utilized as feedstock for the production of fuels, chemicals, etc. (Carbon Capture, Utilization and Storage, CCUS). One way to utilize captured CO_2 is to convert it into methane through the Sabatier reaction (Eq. (1)), employing (green-)H_2:

$$CO_2 + 4\,H_2 \rightarrow CH_4 + 2\,H_2O \quad \Delta H_R^0 = -165\ kJ{\cdot}mol^{-1} \tag{1}$$

The as-obtained e-Methane has gained interest over the years given

* Corresponding author.
** Corresponding author.
E-mail addresses: elisabetta.finocchio@unige.it (E. Finocchio), lidia.castoldi@polimi.it (L. Castoldi).

https://doi.org/10.1016/j.micromeso.2026.114080
Received 14 October 2025; Received in revised form 24 January 2026; Accepted 9 February 2026
Available online 12 February 2026

by the possibility to easily transport it, store it and use it since the natural gas infrastructure is already present, so that it can be injected into the already existing grids for natural gas and utilized as it is. These considerations make appealing the utilization of e-CH_4 as energy carrier (Power-to-Gas), along with the fact that for the already established methanation process, which is performed by co-feeding stoichiometric amounts of CO_2 and H_2 (split 1:4), modern catalysts and plant configurations enable a CO_2 conversion and methane selectivity both close to 100% (>98% [9]), thus requiring condensation of byproduct H_2O as the only needed downstream operation to obtain a grid-compatible product.

The state of the art of methanation catalyst are composed by a hydrogenation metal (Ni, Ru) dispersed over a support (i.e. Al_2O_3, TiO_2, SiO_2, CeO_2). In the literature, the nature of the support has been investigated in relation to the hydrogenation metal activity [10,11], showing that it is strongly related to the support utilized due to electronic or strong metal - support interactions (EMSI or SMSI). Indeed, other than affecting the dispersion and the size of the particles of the catalyst metal, the support actively contributes to the reaction for the adsorption/activation and hydrogenation of CO_2 at the metal - support interface, ultimately modifying the activity and selectivity of the catalytic material.

From a process perspective, traditional CO_2 methanation requires two sequential units, dedicated respectively to the separation and purification of CO_2 and to its methanation, resulting in high Capital Expenditure (CAPEX), along with high Operational Expenditure (OPEX) related to the energy intensive nature of both CO_2 capture (need of temperature/pressure swings [12]) and conversion (necessity of heat management of the exothermic reaction).

To overcome these criticalities, the integration of these two operations in one single reactor has been proposed exploiting the so-called Dual Function Materials (DFMs) [13,14]. Indeed, in this case a stream containing CO_2 (i.e. flue gas, biogas) passes through the catalyst bed where the CO_2 is adsorbed (likely as carbonates); then, by exposing the same catalytic bed to green H_2, the captured CO_2 is converted into methane. This integration is made possible utilizing a catalyst constituted by a support (metal oxide) impregnated with a storage material, typically an alkali/-earth metal oxide, and a methanation metal (Ni, Ru). The co-presence of the active elements over the same support has been proven to provide beneficial effects towards the formation of active storage sites (i.e., due to the Ru-catalysed decomposition of Na_2CO_3 precursor [15]) or due to intimate contact effects that allow increased CH_4 yields [16,17].

Literature research on DFMs has been conducted employing Al_2O_3 as support, mainly due to its great availability and mechanical properties (high surface area, porosity and stability in the range of operation). Arellano-Treviño et al. [18] studied Ni, Ru and Rh as hydrogenation metals identifying Ru as the most promising candidate due to cost effectiveness in comparison with Rh, and reducibility, that ruled out Ni. Indeed, when O_2 is present in the adsorption phase Ni is irreversibly oxidized, so during the subsequent reduction phase the active metallic form has been irretrievably lost. Long term deactivation effects on Ru have been observed by Jeong-Potter et al. [19], reporting irreversible Ru deactivation due to metal sintering after considerable adsorption and reduction cycles. Moreover, they demonstrate that DFMs are able to perform also at Ru loadings as low as 0.5%. The same loss of hydrogenation activity has been observed also by Bermejo-López et al. [20], that reported also the agglomeration of the storage element among the deactivation causes.

The nature of the storage element has been proven to significantly effects the reactivity of these materials [21–24]. Porta et al. [22] investigated different alkaline and alkaline-earth metals, concluding that the highest the basicity of storage elements, the higher the stability of the formed carbonates, leading to uncomplete conversion of the adsorbed species in particular for alkaline-earth metals. The presence of more stable carbonates is positive when the catalyst is tested under flue gas conditions, limiting the competitive adsorption of H_2O.

Regarding the composition of the feed gas, Porta et al. [25] and Bermejo-López et al. [26] reported that the adsorption of CO_2 is inhibited by the presence of O_2 and NO, due to the increased acidity of the latter which leads to a preferential absorption of NO. Therefore, during the reduction phase small amount of CH_4 are obtained while the production of N-compounds such as N_2 and NH_3 is significant.

With the goal of achieving an active and stable formulation, also the effect of the support of DFMs is now starting to attract attention. Several studies of González-Velasco and coworkers [27,28] have explored CeO_2-supported DFMs, particularly Ni- and Ru- based perovskite formulations, showing that CeO_2 enables smaller metal nanoparticles (Ni [27]), higher CH_4 yields, and better stability than Al_2O_3-based systems, where $NiAl_2O_4$ formation negatively affects the redox properties of catalyst. Metal-support interactions are likely behind these performance differences. In agreement, Bracciotti et al. [29] observed an increase in activity and stability towards CO_2 hydrogenation of $In_2O_3/(CeO_2\text{-}ZrO_2)$ compared to In_2O_3/ZrO_2, due to the formation of Ce-Zr-In interfacial sites that enhance In_2O_3 dispersion and inhibit its reduction to metallic In under reaction conditions, possibly due to the oxygen storage capacity provided by Ce^{4+}/Ce^{3+}. Merkouri et al. [30] reported the high activity and selectivity of bimetallic NiRu catalysts supported on CeO_2-Al_2O_3, with near-equilibrium CO_2 conversion, 100% CH_4 selectivity at 350 °C and high stability for traditional methanation reaction. Promoting this catalyst with K results in a DFM with enhanced redox and basic properties due to the ceria-based support. These findings underscore the role of the support regarding redox and surface basicity properties, in regulating both the catalytic activity and adsorption capacity of DFMs. In a recent study by Bahrami et al. [31], the optimization of DFMs was significantly advanced. The authors focused on a Na-Ni-Ru system supported on CeO_2-Al_2O_3, using a Gaussian process surrogate model to navigate the complex interplay between adsorbent loading and catalytic activity. While traditional experimental screening of Na loadings (2.5-15 wt%) indicated that higher adsorbent content generally increased CO_2 desorption capacity, it did not linearly correlate with methane yield. The Research Group identified an optimal Na loading of 7.9 wt%, which achieved a peak methane production of 398.6 μmol/g_{DFM} with the highest selectivity at 400 °C [31].

TiO_2 has been examined by Cimino et al. [32], reporting an enhanced Ru activity towards methanation when supported on TiO_2 rather than Al_2O_3 in agreement with the previous literature [33,34]; on the other hand, the introduction of the storage element (Na or Li) on Ru/TiO_2 results in a detrimental methanation activity, consistent with what previously observed for Al_2O_3-based DFMs [35]. Moreover, in the case of TiO_2-based DFMs the presence of a storage alkaline metal decreases the selectivity to CH_4 with the respect to analogue Al_2O_3-based DFMs; indeed, the interaction between the storage element and TiO_2 modified the basicity of the material, possibly due to electronic interactions thus modifying the selectivity.

Among the other supports, silica (SiO_2) recently has emerged as a widely investigated support material, owing to a combination of physicochemical properties that favor both metal dispersion and stability under reaction conditions. Firstly, silica offers a high specific surface area and a tuneable pore structure, particularly in mesoporous forms. These properties facilitate a high dispersion of active metal sites, such as Ni or Ru [36], and promote efficient mass transport of gaseous reactants and products.

Secondly, SiO_2 is chemically inert and thermally stable, which makes it resistant to structural degradation or undesired chemical interactions during long-term operation. This inertness, while generally unfavourable for direct CO_2 activation due to the lack of basic surface sites, is advantageous when used in conjunction with basic promoters such as alkali or alkaline-earth oxides (e.g., MgO, CaO, BaO) [37]. These additives compensate for the low intrinsic CO_2 affinity of silica by introducing surface basicity, thereby enabling the capture and activation of CO_2 through the formation of carbonate or bicarbonate species.

Finally, silica is abundant, cost-effective, and compatible with

various scalable synthesis methods, making it suitable for industrial catalyst design. Although it lacks the intrinsic CO_2 adsorption capacity of more basic oxides like Al_2O_3 or CeO_2 [18], its modifiability and structural flexibility make it a valuable platform for the development of advanced bifunctional catalysts.

For these reasons, in this work the utilization of silica as support for the integrated CO_2 capture and methanation with DFMs is being investigated through microreactor experiments and FT-IR characterization, to evaluate the surface properties of the SiO_2 supported DFMs and describe the chemistry behind their catalytic activity.

2. Materials and methods

2.1. Catalysts synthesis

The Dual Function Materials have been prepared using commercial silica (BASF, $S_{BET} = 360\ m^2\ g^{-1}$, $V_p = 0.83\ cm^3\ g^{-1}$) as support. Pellets have been grinded and sieved to obtain a powder having a particle diameter between 75 and 106 μm; the powder is then dried at 120 °C overnight.

Incipient wetness impregnation method has been used to prepare Ba-Ru/SiO_2 catalysts. DFMs have been prepared by impregnating via wetness impregnation the dried SiO_2 support with a solution of ruthenium nitrosyl nitrate (Alfa Aesar, commercial solution 1.5% $g_{Ru}{\cdot}mL^{-1}$), dosed to obtain a 0.5 wt% of Ru. The obtained material is then dried at 100 °C for 12 h and then calcined at 500 °C for 5 h (2 °C·min^{-1} heating ramp). The so-obtained Ru/SiO_2 sample. has been impregnated with a solution of barium acetate (precursor salts from Sigma Aldrich, ACS reagent, 99% purity) to obtain a barium loading of 16 wt%. After drying at 100 °C for 12 h and calcination at 500 °C for 5 h (2 °C·min^{-1} heating ramp) a Ba-Ru/SiO_2 DFM is finally obtained.

A similar preparation method has been used, reversing the order of impregnation: at first, Ba is dry impregnated on SiO_2 (16 wt% load, Barium acetate precursor). After drying (100 °C, 12 h) and calcination (500 °C, 5 h, 2 °C·min^{-1} heating rate), the so-obtained Ba/SiO_2 sample has been dry impregnated with ruthenium nitrosyl nitrate (0.5 wt%) and finally just dried at 120 °C overnight to obtain a Ru-Ba/SiO_2 DFM. This last procedure has been performed also to prepare a DFM with increased Ba loading (32 wt%), namely Ru-32Ba/SiO_2. Synthesis procedures have been chosen according to results previously published [22,25].

The list of prepared catalysts together with their composition is reported in Table 1. The nominal content of Ru and Ba was confirmed through EDX analysis (Table S1).

2.2. Catalysts characterization

The prepared catalysts have been characterized in terms of morphology, chemico-physical properties, and catalytic activity in CO_2 methanation.

Brunauer-Emmett-Teller (BET) analysis was performed by adsorption-desorption of nitrogen at −196 °C using a Micrometrics Tristar 300 instrument. Prior to the measurement all samples were outgassed under vacuum at 120 °C for 3 h. Specific surface areas and adsorption–desorption isotherms calculated by Brunauer–Emmett–-Teller, and Barret–Joyner–Halenda (BJH) method, respectively from the adsorption and desorption branch of the isotherm data.

Table 1
Nominal metal content, morphological characterization results of prepared DFMs.

Sample	Ru-loading (wt.%)	Ba-loading (wt.%)	S_{BET} ($m^2 \cdot g_{DFM}^{-1}$)	V_P ($cm^3 \cdot g_{DFM}^{-1}$)	$d_{p,avg}$ (nm)
SiO_2	0	0	360	0.83	8.8
16Ba/SiO_2	0	16	212	0.60	10.8
0.5Ru/SiO_2	0.5	0	353	0.81	8.9
16Ba-Ru/SiO_2	0.5	16	180	0.52	11.3
Ru-16Ba/SiO_2	0.5	16	128	0.47	14.7
Ru-32Ba/SiO_2	0.5	32	87	0.29	13.7

X-Ray diffraction (XRD) patterns were collected using a Panalytical diffractometer (Empyrean model) in Bragg–Brentano geometry fitted with a copper tube (Cu Kα radiation). The data sets were acquired in continuous scanning mode over the 2 θ range 5 – 70°, using a step interval of 0.0260° and step time of 110 s. Inorganic Crystalline Structure Database (ICDS) has been used to recognize the crystalline phases.

Skeletal Fourier Transform Infrared Spectroscopy (FT-IR) spectra of catalyst powders have been recorded in a Nexus FT-Instrument (ThermoNicolet) equipped with a ATR accessory (diamond window), collecting 100 scans with a resolution of 4 cm^{-1} and background air (DTGS detector and OMNIC software).

H_2-TPR has been performed using a TPDRO 1100 instrument (ThermoFisher) to assess the reducibility of the fresh materials by feeding 5% H_2/Ar from room temperature to 500 °C (heating at 10 °C·min^{-1}). Ru dispersion was obtained through H_2 chemisorption using the same equipment, performed through pulsing 5% H_2/Ar at 100 °C on the reduced samples. The values of Ru dispersion and particle dimension have been calculated using correlations provided by Bergeret et al. [38], which have been reported in the supplementary material. The reduced samples are then passivated in O_2 (2% O_2, 1h at room temperature) and characterized with the previously mentioned techniques.

Adsorption and desorption experiments have been carried out in transmission mode over pure powder disks (25 mg average disks weight) directly in the IR cell connected to a conventional gas manipulation apparatus. For these experiments as well as CO_2-TPD, H_2-TPSR and H_2-CO_2 cofeeding tests, described in the following, the same FT-IR instrument was used (DTGS detector, 100 scans, 4 cm^{-1} resolution and OMNIC software). Before any adsorption experiment, samples were activated in vacuum (10^{-3} Torr) for 1h at 500 °C or reduced at the same temperature in hydrogen and subsequently outgassed at 500 °C (Ru/Ba sample). PY adsorption was performed at room temperature over the activated samples and spectra of the surface species were recorded at each desorption step in the range 150-400 °C. CO adsorption has been carried out employing a specific quartz cell with an external chamber for liquid nitrogen with a thermocouple located in a specific position near the self-supported disk sample. Tests were performed at liquid nitrogen temperature and spectra were recorded upon outgassing at increasing temperature by progressive removal of liquid nitrogen from −140 °C to room temperature or higher.

FT-IR CO_2 adsorption and desorption in programmed temperature (CO_2-TPD) experiments were performed by introducing into the IR cell 18 Torr of pure CO_2 at room temperature and following outgassing at R. T. during 1h. Subsequently, spectra of the surface species were recorded at each desorption T-step in the range 150-500 °C.

FT-IR H_2 temperature programmed surface reduction (H_2-TPSR) tests were carried out by employing the same instrument and conditions described above. After CO_2 adsorption phase and outgassing at room temperature, 140 Torr of pure hydrogen were introduced in the IR cell at room temperature, and then spectra of the surface species and gas phase were recorded at each temperature in the range 150-500 °C maintaining H_2-atmosphere. The CO_2 capture step was carried out at low temperature [31,39] due to the thermodynamic advantage of adsorption under these conditions.

In another set of experiments, FT-IR CO_2-H_2 cofeeding experiment were performed. A mixture of CO_2/H_2 (excess H_2) was added in the IR cell on the pre-reduced Silica-based sample. Spectra of gas-phase species and spectra of surface species were recorded at 200, 250, 300, 350 and 400 °C and after outgassing at room temperature following reaction.

2.3. Catalytic activity

Catalytic testing was performed loading 60 mg of sieved catalyst (75-106 μm particle diameter) in packed bed quartz microreactors (7 mm internal diameter).

Temperature was monitored and controlled by using a K-type thermocouple positioned in the center of the catalytic bed. The composition of the gas phase exiting the reactor was continuously analyzed with a mass spectrometer (Pfeiffer Vacuum QMS200 quadrupole, analysis every 4s) and a micro gas chromatograph (Agilent 3000, analysis every 180s).

The inlet flowrate of the experiments was set to 100 mL(STP)·min^{-1}, resulting in a space velocity of 100 L(STP)·h^{-1}· g_{DFM}^{-1}. The flowrate was kept constant also when introducing reagent gases in the reactor (i.e. CO_2, H_2) by using two six-way valves, allowing to obtain a precise pulse when switching gases.

Different experiments have been performed to evaluate the catalytic performances of the catalysts: CO_2 Temperature Programmed Desorption (CO_2-TPD) and Temperature Programmed Surface Reaction (H_2-TPSR). Before each experiment, the catalyst was pretreated under H_2 atmosphere (4% v/v in He) at 500 °C (heating rate of 10 °C·min^{-1}) to remove eventual adsorbed species.

CO_2-TPD tests were carried out after the samples were saturated with CO_2 by feeding a stream containing CO_2 (1% v/v in He) at 150 °C for 15 min. Eventually, the CO_2 flow was switched off and the temperature was increased to 500 °C in He (heating rate of 10 °C·min^{-1}). In the H_2-TPSR experiment, after CO_2 adsorption (in the same conditions as CO_2-TPD), H_2 (4% v/v in He) has been fed to the reactor, and the temperature was increased to 500 °C in He (heating rate of 10 °C·min^{-1}).

The quantitative evaluation of the evolved species was determined by integrating the concentration profiles over time during the TPD and TPSR tests, as described by Eq. (1):

$$\left[\frac{\mu mol_i}{g_{DFM}}\right] = \int C_i dt \cdot \frac{Q}{22.414} \cdot \frac{1}{g_{DFM}} \quad \text{Eq. 1}$$

where g_{DFM} refers to the amount of fresh DFM-sample loaded in the reactor, C_i is the concentration of *i*-species (i = CO_2, CO, CH_4) measured during each run (ppm), t is the time (s) and Q is the total volumetric flow rate (mL·min^{-1}) measured at standard temperature and pressure conditions (298 K and 1 atm).

3. Results and discussion

3.1. Catalyst characterization

N_2 adsorption – desorption analysis **-** Isotherms are reported in Fig. 1. Bare SiO_2 and DFMs exhibit type IV physisorption isotherms and type H3 hysteresis loops [40]; moreover, the pore size distribution reveals a single main peak for all the catalysts.

As reported in Table 1, the surface area of the bare silica decreased considerably upon Ba addition, whereas the effect of Ru incorporation was negligible, as also observed in the literature [41].

Moving from binary catalyst (i.e Ru/SiO_2) to DFM one (i.e Ba-Ru/SiO_2), whatever the impregnation order is, it is possible to observe a reduction in both surface area and pore volume, in line with literature results on similar ternary catalysts [22], while the average pore diameter remained between 11.3 and 14.7 nm. Notably, when the first impregnation step is with barium, the decrease in the surface area is greater (128 versus 180 m^2· g_{cat}^{-1}), possibly due to the direct incorporation of Ba species into the silica pores, as evidenced by the slight decrease in pore volume. This results more evident at higher Ba loading (e.g. 32% w/w).

X-ray diffraction **-** XRD patterns recorded for commercial silica and all the bimetallic DFMs are reported in Fig. 2. The monometallic samples, 16Ba/SiO_2 and Ru/SiO_2, exhibited only slight modifications compared to the typical amorphous silica pattern of the support. In particular, 16Ba/SiO_2 displayed diffraction reflexes corresponding to the orthorhombic phase of $BaCO_3$ (witherite, JCPDS No. 5-378) at 23.9°, 24.2°, 34.6°, 41.9°, and 44.8°. These peaks increased in intensity over time when the samples were aged under ambient conditions, a phenomenon already reported in the literature [25,42].

Ru/SiO_2 sample exhibited very weak diffraction lines at 28.1°, 35.1°, 40.0°, and 54.3° attributable to RuO_2 tetragonal phase (JCPDS No. 43-1027); the very low intensity could be due to the tiny amount of metal (i.e. 0.5% wt.) and/or to the small RuO_x crystallite size.

In all the bimetallic samples, containing both Ba and Ru (Fig. 2d-f, and S1), the XRD patterns were similar, showing pronounced peaks corresponding to $BaCO_3$ witherite-phase. The XRD pattern reported in the literature for an analogous 16Ba-Ru sample supported on γ-Al_2O_3 agrees with our results indicating that carbonate species are predominant [25]. It should be noted that the diffraction features related to the RuO_2 phase are largely masked by the intense Ba-carbonate peaks, with only the diffraction at 40.0° and 54.3° detectable, although very weak, due to the low Ru concentration in these samples.

IR characterization **-** Fig. 3 reports the ATR - IR skeletal spectra of

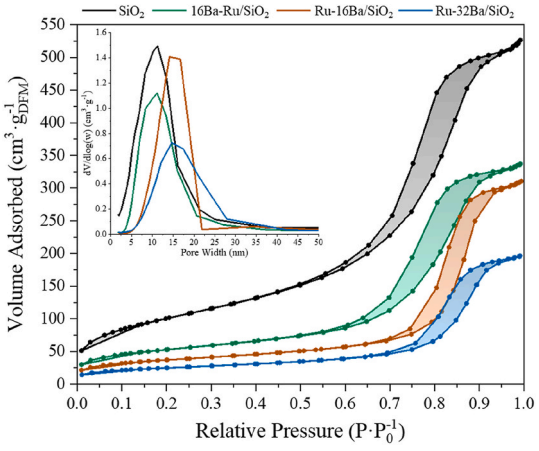

Fig. 1. N_2 adsorption-desorption isotherms at 77 K and pore size distribution for the investigated samples.

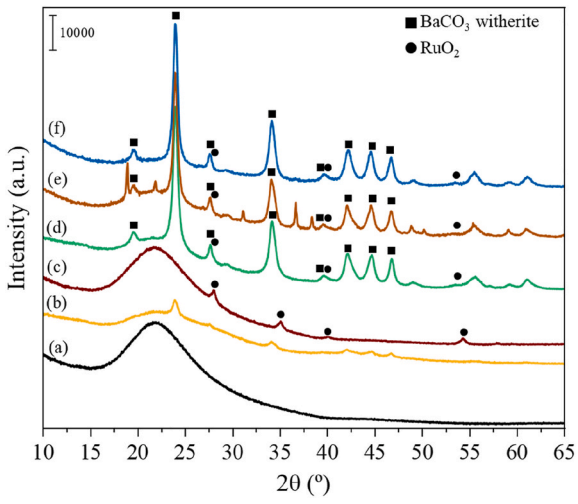

Fig. 2. XRD patterns of (a) SiO_2, (b) 16Ba/SiO_2, (c) Ru/SiO_2, (d) 16Ba-Ru/SiO_2, (e) Ru-16Ba/SiO_2 and (f) Ru-32Ba/SiO_2.

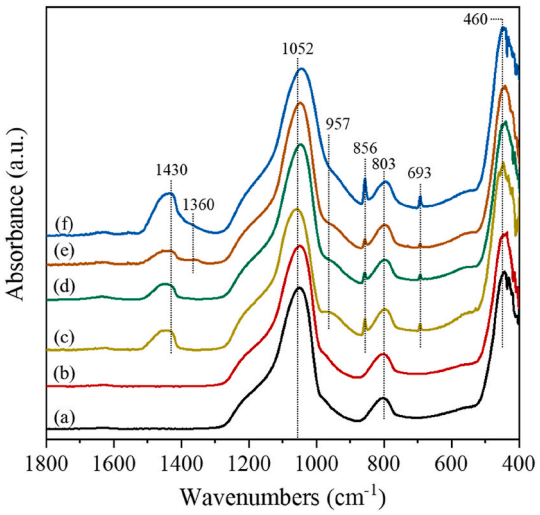

Fig. 3. ATR FT-IR spectra of (a) SiO_2, (b) Ru/SiO_2, (c) $16Ba/SiO_2$, (d) $16Ba\text{-}Ru/SiO_2$, (e) $Ru\text{-}16Ba/SiO_2$ and (f) $Ru\text{-}32Ba/SiO_2$.

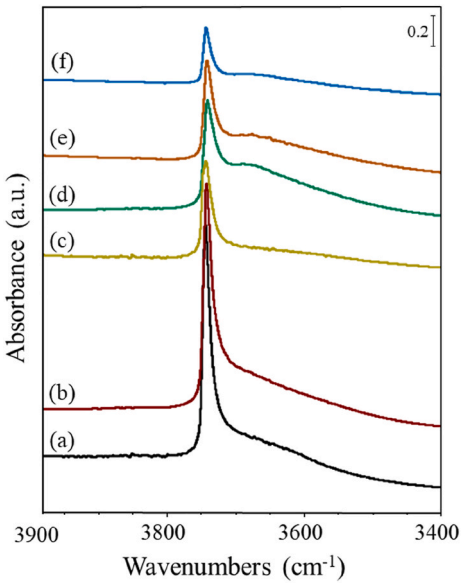

Fig. 4. OH stretching region FT-IR spectra of (a) SiO_2, (b) Ru/SiO_2, (c) $16Ba/SiO_2$, (d) $16Ba\text{-}Ru/SiO_2$, (e) $Ru\text{-}16Ba/SiO_2$ and (f) $Ru\text{-}32Ba/SiO_2$ after activation at 500 °C for 1 h.

prepared DFMs where all the spectra intensities are normalized to the Si-O structural main band. The spectra show typical peaks around 1050 cm^{-1} (broad), 800 cm^{-1} and 460 cm^{-1}, due to the IR-active vibrational fundamental modes of silica related to the asymmetric stretching and symmetric stretching and bending modes of Si-O-Si bonds organized in SiO_4 tetrahedron (Fig. 3, spectrum a) [43]. These features are similar in the spectra of all silica-supported samples, regardless of the preparation procedure.

The pronounced shoulder detected between 980 and 950 cm^{-1} has been reported to be due to the Si-OH vibrational mode and sensitive to surface modifications [44]. Its significant intensity is consistent with the presence of exposed silanol groups still detectable after the incorporation of Ba and Ru promoters. Indeed, these cations do not enter significantly the bulk structure due to the preparation method chosen and to the mild calcination temperature (i.e. 500 °C).

After Ba addition (Fig. 3, spectrum c), several new bands in the region 1500-600 cm^{-1} are detected, namely at 1430, 856 and 693 cm^{-1}, typical of presence bulk carbonate ions [45]. As reported also for other materials [46] this suggests that the presence of these cations at the surface is associated with that of corresponding oxide ions, which are characterized by surface high basicity. This leads to the formation of carbonate ions by adsorption of CO_2 from the environment and/or after calcination of the acetate Ba precursor.

These features are common to all samples, regardless of the order of impregnation of Ba and Ru (compare Fig. 3, spectra d and e). Moreover, when the barium loading was increased (Fig. 3, spectrum f), the [$BaCO_3$-bulk]:[Si–O–Si] intensity ratio correlated well with the higher loading of the storage element, being 3.5 times greater than that calculated for samples containing 16 wt% Ba. Thus, an increased promoter loading preferentially leads to the formation of bulk-type $BaCO_3$ species upon calcination, while the impregnation order did not influence the surface density of these species.

To complete the superficial characterization, the OH stretching region has been analyzed by FT-IR after outgassing at 500 °C for 1h and the results are reported in Fig. 4.

Silica spectrum is consistent with literature reports, showing the cut off at 1300 cm^{-1}, typical of silica-based materials, overtones of bulk vibrations in the region 2100-1500 cm^{-1} and the sharp band of the OH stretching mode of free-surface silanols at 3745 cm^{-1} [47] (see Fig. S1). The latter band is reduced in intensity in the spectrum of the Ba-containing samples and appears more complex. The addition of Ru does not introduce significant modifications in the silica OH groups, likely due to the very low amount of the metal, while a further reduction in intensity of this band is observed in the spectrum of the sample at the highest Ba loading (Fig. 4, spectrum f). This observation provides evidence of the perturbation of the surface by oxide species, which limits the amount of exposed silanols and induces some heterogeneity of the surface hydroxyls. Apparently, the sequence of the impregnation procedure does not affect the surface properties of this system. As discussed in the previous section, bands due to surface and bulk carbonate species are detected in the low frequency region (1600-1300 cm^{-1}) in the samples containing Ba oxides, clearly indicating the basic character of this surface (see Fig. S1).

Reducibility characterization - Information on the reducibility of the catalytic samples was obtained through H_2-TPR experiments, as reported in Fig. S2. $16Ba\text{-}Ru/SiO_2$ (Fig. S2 a) shows the onset of reduction at 185 °C, with a main reduction peak centered at 260 °C likely associated with the reduction of residual barium carbonates formed during calcination. This interpretation is supported by the XRD pattern of the reduced and passivated $16Ba\text{-}Ru/SiO_2$ sample (Fig. S3), which differs significantly from the fresh material (Fig. 2): the disappearance of the crystalline $BaCO_3$ reflections indicates its transformation into amorphous compounds (i.e., BaO), along with the presence of crystalline Ru^0. Results of N_2 physisorption carried out on the reduced $16Ba\text{-}Ru/SiO_2$ sample show an increased BET surface area compared to the fresh material (reduced: 220 $m^2 \cdot g_{DFM}^{-1}$ vs fresh: 180 $m^2 \cdot g_{DFM}^{-1}$), consistent with the decomposition of the $BaCO_3$ phase. No significant changes in the shape of the physisorption isotherm and pore size distribution are observed on the reduced sample (Fig. S4).

In contrast, $Ru\text{-}16Ba/SiO_2$ sample (Fig. S2 b) begins to reduce at lower temperature (125 °C) and presents a higher H_2 consumption compared to the previous material. This increased H_2 consumption is attributed to the first thermal treatment carried out in the presence of both Ru and Ba, consistent with the catalytic decomposition of the storage element by Ru [15]. In this case, three distinct reduction peaks are observed and can be tentatively assigned to the reduction of Ru (210 °C), residual Ba nitrates (360 °C) and Ba carbonates (450 °C). The continued H_2 consumption after holding the temperature at 500 °C suggests that the reduction of $BaCO_3$ remains incomplete following the activation procedure, leaving residual crystalline $BaCO_3$ (Fig. S3). The presence of crystalline $BaCO_3$ after reduction is reflected in the BET surface area, which remains essentially identical to that of the fresh material (reduced: 127 $m^2 \cdot g_{DFM}^{-1}$ vs fresh: 128 $m^2 \cdot g_{DFM}^{-1}$). As in the

previous case, no significant changes in the shape of the physisorption isotherm and pore size distribution are observed (Fig. S4).

The same three peaks of H_2 consumption observed with Ru-16Ba/SiO_2 are present also with Ru-32Ba/SiO_2, although the peaks associated with Ru reduction and carbonate reduction appear more intense and are shifted to higher temperatures (respectively, 280 °C and 480 °C). This behavior is expected due to the higher Ba loading in the material.

The dispersion of Ru was determined by H_2 chemisorption pulse experiment for 16Ba-Ru/SiO_2, Ru-16Ba/SiO_2 and Ru-32Ba/SiO_2 samples and included in Table S1, along with the corresponding calculated average Ru particle dimension. The lower Ru dispersion observed for 16Ba-Ru/SiO_2 compared to Ru-16Ba/SiO_2 might be attributed to the calcination procedure applied on the former after the Ru impregnation step.

Acidity characterization **-** The acidity properties of the catalytic surface have been investigated by FT-IR spectroscopy using pyridine as probe molecule. The resulting spectra after outgassing at 150 °C are reported in Fig. 5 for bare SiO_2, Ru/SiO_2 and Ru-16Ba/SiO_2 as exemplification of different formulations.

Silica is a weak protonic acid, so adsorption of pyridine and its following desorption at 150 °C gives rise to weakly adsorbed species, characterized by IR bands at 1597 and 1446 cm^{-1} due to H-bonded pyridine molecules interacting with surface silanols. Correspondingly, stretching bands of isolated OH groups appear as negative features in the subtraction spectra, giving rise to a broad absorption centered near 3500 cm^{-1} (see also Fig. S5).

The modification with Ba ions increases the basicity of the surface, and also appears to add Lewis acidity, as revealed by the weak band at 1617 cm^{-1} due to pyridine molecules coordinated over medium strength Lewis sites (Fig. 5, spectra b and c) [48,49]. Also in this spectrum, silanol groups still exposed at the surface allow interaction through H bonds, as revealed by the negative band in the high frequency region of the IR spectrum (see Fig. S5). In parallel, bands due to H-bonded pyridine appear at 1596 cm^{-1}. The same conclusions apply to the surface of the Ru-containing catalyst (Fig. 5, spectrum c), where some Lewis acidity can be related to the Ru ions, although in negligible amount due to the very low loading of the metal.

CO adsorption and FT-IR characterization **-** CO adsorption at low temperatures has also been carried out over the SiO_2 and Ba/SiO_2 samples. The spectrum of CO adsorbed over silica (see Figure S6 a) shows a main sharp band at 2156 cm^{-1} (CO stretching region), due to CO weakly interacting with the support through H-bonds, together with a pronounced shoulder at ~2139 cm^{-1}, due to the presence of liquid-like CO. Outgassing at increasing temperature (from −140 °C to 150 °C) results in the rapid disappearance of both components, according to their weak interaction with the surface. The main features described above are present also in the spectra of CO adsorbed over the Ba-containing silica (Figure S6 b); however, after outgassing, the wavenumber of the former components shifts to higher values (from 2157 to 2168 cm^{-1}), according to the behavior of CO adsorbed over metal oxides ions. These results are in good agreement with those of pyridine adsorption, confirming that metal ions generate Lewis sites exposed at the surface.

Low temperature CO adsorption has also been carried out over the reduced Ru-16Ba/SiO_2 sample and the corresponding spectrum is shown in Fig. 6. Starting from −140 °C a very complex pattern of IR features due to carbonyl species is detected. The main band centered at 2155 cm^{-1} and quickly disappearing following outgassing is related to CO interacting with the hydroxyl groups of silica. A broad band centered at 2053 cm^{-1} with shoulders near 2000 cm^{-1} and 2100 cm^{-1} is observed, assigned to (multi)carbonyl species [$Ru^{n+}(CO)_{2\text{-}4}$], having a partially oxidized character, and to linearly adsorbed CO on Ru^0 species, likely isolated and defective sites. Another weak component at 2137 cm^{-1}, together with a shoulder near 2090 cm^{-1}, can also characterize carbonyls coordinated on partially oxidized Ru and on Ru ions [50].

By increasing the temperature, i.e. by lowering the CO coverage, the high frequency components are almost completely lost, and the 2053 cm^{-1} band broadened and shifted to lower frequencies. At 100 °C, a broad absorption is still detectable, centered at 2038 cm^{-1} together with a further broad shoulder extending in the 2000-1950 cm^{-1} region and likely associated with bridging species. This band shifting upon outgassing is due to carbonyls adsorbed on extended Ru metal particles, whose frequency decreases at low CO coverage due to the well-known coupling effects [50].

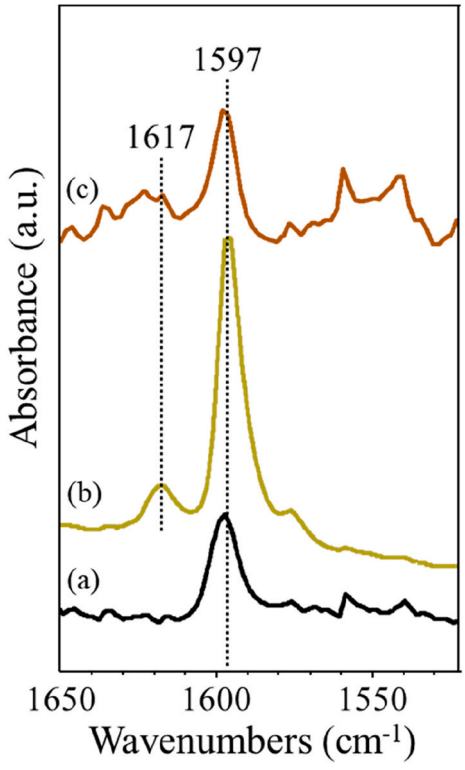

Fig. 5. FT-IR subtraction spectra of surface species after desorption of pyridine at 150 °C and outgassing at 150 °C: (a) SiO_2, (b) 16Ba/SiO_2 and (c) Ru-16Ba/SiO_2 (enlarged). The activated spectrum was subtracted.

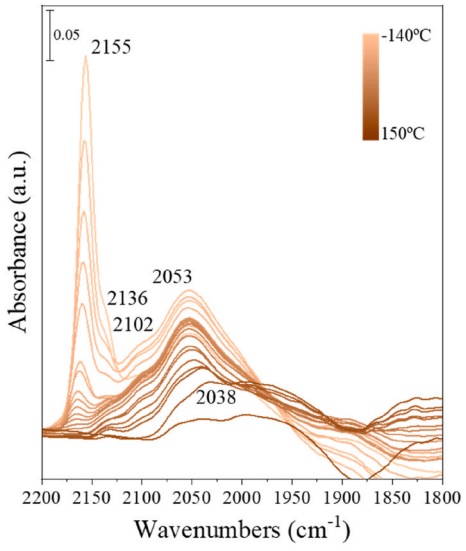

Fig. 6. FT-IR spectra of surface species arising from low temperature CO adsorption over Ru-16Ba/SiO_2 and following outgassing from -140 °C up to 150 °C. The activated surface spectrum was subtracted.

These data indicates that even after reduction in hydrogen cationic Ru species can be detected, likely interacting with the support. At the same time, small amounts of isolated or clustered Ru metal particles (bands in the 2100-2000 cm^{-1} range) and large metal particles (2060-2030 cm^{-1}) are also observed.

Co-feeding CO_2/H_2 - The co-feeding of CO_2 and hydrogen has been directly carried out in the IR cell at high temperatures, in order to study the state of active Ruthenium in an atmosphere mimicking the methanation reaction. The results obtained over Ru-16Ba/SiO_2 catalyst are reported in Fig. 7. In these conditions, the formation of gaseous CH_4 together with CO traces has been detected in the IR cell in the temperature range from 250 °C to 400 °C (Fig. 7A), showing the capability of this catalytic system to perform a non-selective CO_2 reduction. IR Spectra of the surface species shows a sharp band at 2345 cm^{-1} due to linearly adsorbed CO_2 (OCO asymmetric stretching) decreasing in intensity during the reaction. A mixture of bicarbonate and carbonate species (bands at 1650, 1588, 1452 and 1391 cm^{-1}) formed and coordinated on barium centers, whose intensity increases at increasing temperature, is also detectable. The peak at 1622 cm^{-1} is due to vibrational mode of adsorbed water, increasing in intensity as a product of methanation reaction in the IR cell.

As soon as CO is formed, i.e. between 200 °C and 250 °C, the main feature in the IR spectrum is a broad and complex band centered at 2030 cm^{-1}, with shoulders at 2000 cm^{-1} and possibly 2045 cm^{-1} (Fig. 7B and magnification) characterizing strongly adsorbed CO species. A broad and weak absorption at about 1895 cm^{-1} is overlapping with overtone features of the silica support.

The 2030 cm^{-1} band (LF band) has been typically assigned by several authors to carbonyl species linearly coordinated over reduced, metallic Ru particles, in agreement with the band position characteristic of CO adsorption on Ru single crystals [51]. The complexity of the band suggests the presence of several Ru species exposed at the surface and revealed already at such low CO coverage. Namely, the presence of the poorly resolved shoulders at frequencies higher than 2050 cm^{-1} could be due to (multi)carbonyl species on Ru having a partially oxidized character [52] and to linearly adsorbed CO on high energy defects sites and isolated Ru^0 species surrounded by partially oxidized Ru [53]. The component below 2000 cm^{-1} has been associated with another, more labile, on-top carbonyl species [50]. In the temperature range 250-350 °C, CO and methane formation are increasing in the gas phase (Fig. 7A) and consequently, the carbonyl coverage increases at the surface [35]. Features of carbonyl species become sharper and stronger, and apparently low frequency components are almost lost. Possibly, a shoulder near 2070 cm^{-1} grows and can be evidenced in the magnification spectrum (Fig. 7B). Such a high frequency component could be related again to carbonyls coordinated over partially oxidized Ru [53]. The predominance of the LF band on the other features, identified as carbonyl species on partially oxidized Ru, is a consequence of the differences in the dispersion of the metal phase. As a matter of fact, the appearance of several CO adsorption bands in the 2100-2000 cm^{-1} spectra region has always been related to metal particle size. For instance, the presence of three CO bands has been reported when CO was adsorbed on finely dispersed Ru-alumina samples with particle size less than 60 Å, but for CO adsorption on a sample with particle size greater than 90 Å, only one band was seen [54]. Bands of adsorbed water are detected at 1622 cm^{-1} (deformation mode of H_2O [55]) and in the range 3200-3600 cm^{-1} (spectral region not shown). In this spectral region several components can be highlighted: at 3630, 3550 and 3050 cm^{-1} due to stretching modes of OH groups of the silica support involved in H-bonds and to adsorbed water. Finally, the decrease in intensity of the bridging band in favor of the linear carbonyl species is also completely consistent with the increasing CO coverage. It is interesting to note that no HF bands can be detected above 2100 cm^{-1} diagnostic of $Ru^{n+}(CO)_{2\text{-}4}$ species, suggesting that CO induced oxidation of Ru does not occur on the silica barium catalyst, even at such high temperature [56].

Summarizing, conditioning the catalyst surface in these experimental conditions, i.e. a strongly reducing environment and high temperatures, results in a low dispersion of supported ruthenium particles, which become smoother (less defective) than those detected following hydrogen reduction of the sample. resent of an electron-donating effect from the basic O^{2-} species of the Ba oxide. Also, the presence of water vapor arising from methanation of CO_2 can cause agglomeration of the Ru particles (see the growing of methane diagnostic band at 3015 cm^{-1} in the gas phase spectra [55].

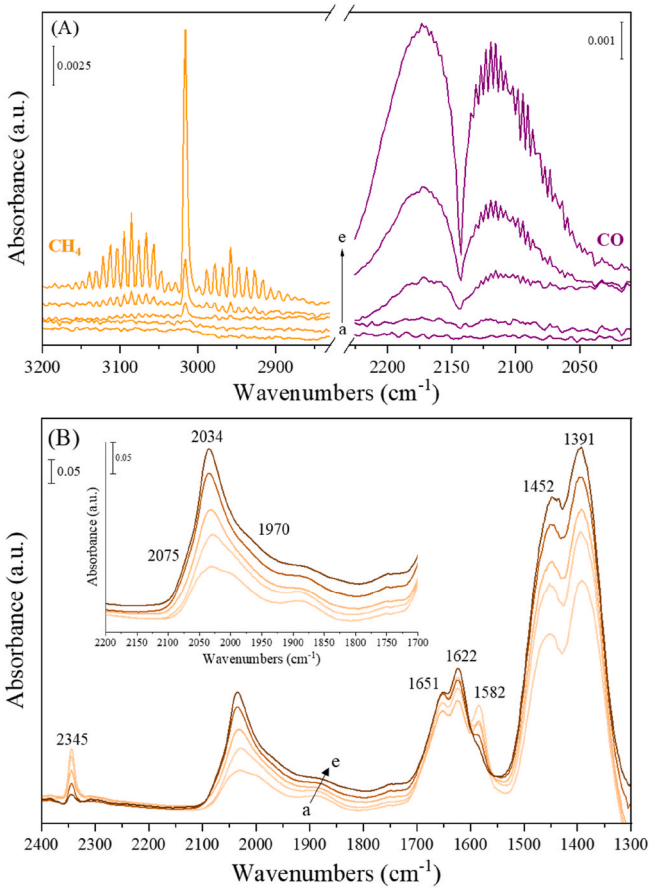

Fig. 7. (A) gas phase FT-IR spectra and (B) surface FT-IR spectra of Ru-16Ba/SiO_2 catalyst in CO_2 + H_2 at increasing temperatures from (a) 200 °C to (e) 400 °C (50 °C/step).

3.2. *DFMs methanation activity*

The catalytic activity of DFMs has been evaluated by means of microreactor experiments combined with FT-IR spectroscopy in order to elucidate the superficial features that could justify the observed behaviors. Note that only the sample containing both Ru and Ba exhibit CO_2 desorption capacity.

3.2.1. *CO_2 temperature programmed desorption (CO_2-TPD)*

CO_2-TPD experiments have been carried out over all the ternary DFMs. Fig. 8 shows the evolution of the CO_2 concentration profile as a function of temperature up to 500 °C after CO_2 adsorption; the corresponding amounts of desorbed CO_2 are reported in Table 2.

In general, it is possible to identify three distinct desorption regions: a low-temperature region (150-280 °C), a medium-temperature region (up to 350 °C), and a high-temperature region (up to 500 °C). This suggests the presence of distinct carbonate species with varying thermal stability and strength, with the low- and medium-strength species being the predominant carbonate population, while the species that remained adsorbed at temperatures above 350 °C were less abundant.

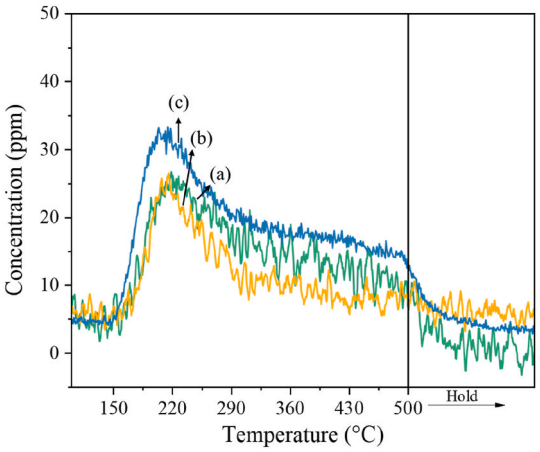

Fig. 8. CO_2-TPD profiles for (a) 16Ba-Ru/SiO_2, (b) Ru-16Ba/SiO_2 and (c) Ru-32Ba/SiO_2.

Table 2
CO_2 adsorption capacity of DFMs samples.

Sample	$CO_2^{desorbed}$-TPD ($\mu mol \cdot g_{DFM}^{-1}$)	$CH_4^{produced}$-TPSR ($\mu mol \cdot g_{cDFM}^{-1}$)	$CO_2^{produced}$-TPSR ($\mu mol \cdot g_{DFM}^{-1}$)
16Ba-Ru/SiO_2	42	37	0
Ru-16Ba/SiO_2	41	34	0
Ru-32Ba/SiO_2	56	53	11

In all cases, the CO_2 desorption profile exhibited a broad desorption peak with a maximum between 200 °C and 230 °C, showing a decreasing desorption trend with increasing temperature. After reaching 500 °C, almost all the adsorbed species are decomposed (C-balance close within 10%). Note that the impregnation of barium at first lowered the CO_2 desorption maximum (compare curve a and b), suggesting that a higher amount of weak basic sites are present on the Ru-16Ba/SiO_2 than on the 16Ba-Ru/SiO_2 sample (see FT-IR results discussed below).

When the barium loading increases (from 16% to 32% wt, Fig. 8, curve c), the CO_2 desorption profile becomes more complex, suggesting a different array of carbonate species. Indeed, thermal desorption occurs mainly between 200 °C and 450 °C and the amount of CO_2 released stays steady up to 500 °C, indicating that higher temperatures are needed to completely desorb the carbonates, so the sample mainly has medium to strong basic properties.

As reported in Table 2, the amount of CO_2 desorbed (used as a measure of the storage capacity) is 42 $\mu molCO_2 \cdot g_{cat}^{-1}$. Furthermore, by increasing the Ba loading, the desorbed CO_2 increases as well. Note that the impregnation order does not seem to affect the CO_2 storage capacity.

The nature and thermal stability of the species formed upon CO_2 adsorption were studied for the SiO_2-based samples using FT-IR spectroscopy. To ensure maximum adsorption, the samples activated in vacuum were saturated with CO_2 at room temperature before being subjected to outgassing with increasing temperatures from 150 °C to 500 °C. The resulting subtracted spectra are presented in Fig. 9 in the region above the cut-off of silica support. Note that 16Ba-Ru/Al_2O_3 has been reported also for comparison purposes.

CO_2 adsorption-desorption FT-IR test performed on 16Ba/SiO_2 (Fig. S7) already shows the formation of a complex system of species, summarized in Fig. 10, within the carbonate region (1800-1320 cm^{-1}). A band at 1690 cm^{-1} is attributed to the initial formation of weakly adsorbed bicarbonate species associated with interactions with hydroxyl groups of basic element, likely present at the catalyst surface [45], and disappeared after mild outgassing. Bands centered at 1650, 1620, 1462, and 1378 cm^{-1} were detected and assigned to various surface carbonate species of the bidentate chelate type [45,57,58] formed on the Ba oxide.

Similar signals were observed in the case of Ru-Ba-containing catalysts. For the 16Ba-Ru/SiO_2 sample, i.e. Ru impregnated first (Fig. 9A), exposure to CO_2 at room temperature resulted in the formation of a complex system of species within the carbonate region. A band at 1690 cm^{-1}, is attributed to the initial formation of weakly adsorbed bicarbonate species associated with interactions with hydroxyl groups of basic dopant and oxides on silica [45] disappearing after mild outgassing. Bands centered at 1650, 1620, 1495, and 1378 cm^{-1} were detected and assigned to various surface carbonate species of the bidentatfinde chelate type [48,58,59] formed on the Ba oxide. The band at 1378 and 1495 cm^{-1}, attributed to a strongly bonded bidentate chelate species, were observed upon CO_2 exposure and subsequent quick degassing. Additionally, a shoulder at 1347 cm^{-1}, attributed to weaker adsorbed monodentate surface carbonates [59], was also observed disappearing after outgassing for 1 h and was completely absent at higher temperatures. Although the intensities of the 1650 and 1620 cm^{-1} bands decreased slightly by increasing temperature up to 150 °C were still detectable while 1495 and 1380 cm^{-1} bands were maintained. As the temperature increased, chelating bidentate carbonate-species features gradually diminished, and a new broad peak emerged at 1550 cm^{-1}, attributed to bridging bidentate carbonate species [25,45,46,59], suggesting an evolution from bidentate chelating carbonates into bridging bidentate species with temperature still observable at 500 °C.

In particular, analyzing the influence of the precursor impregnation order by first impregnating the alkali(-earth) and subsequently the noble metal (i.e. Ru-16Ba/SiO_2, Fig. 9B), a peak at 1495 cm^{-1} was also observed upon CO_2 exposure and subsequent quick degassing. This band is attributed to a strongly bonded bidentate chelate species possibly resulting from the interaction between Ba and Ru oxide species. The peak at 1378 cm^{-1} can be assigned to an even stronger chelating bidentate carbonate species related to BaO-phase close to Ru-atoms. Additionally, a shoulder at 1347 cm^{-1}, attributed to weaker adsorbed monodentate surface carbonates, was also observed [59,60]. After 1 h of outgassing and heating to 150 °C, the 1690 cm^{-1} and 1347 cm^{-1} bands, weakly bonded bicarbonate and monodentate carbonates respectively, disappeared, confirming the complete removal of these species, the intensities of the 1650 and 1620 cm^{-1} bands slightly decreased, while the 1495 and 1380 cm^{-1} bands, corresponding to more strongly adsorbed bidentate chelated carbonates, maintained their intensity. Also, the band at 1650 and 1620 cm^{-1} gradually diminished, and a new broad peak emerged at 1550 cm^{-1} attributed to bridging bidentate carbonate species but not observable at 500 °C suggesting when the Ba promoter is added onto Ru (Ba-Ru), the probability of the presence of isolate BaO phase domains at the surface increases together with the formation capability of stable carbonate species which require higher temperatures to desorb compared to Ru-Ba.

The modified stability of Ba carbonate species is expected to correlate with the preparation method. Since the Ru precursor solution contains nitric acid, its impregnation over Ba/SiO_2 leads to the chemical decomposition of Ba carbonates formed during calcination of the acetate precursor. As a result, Ba nitrates are generated, which decompose more readily into BaO in presence of H_2 (i.e. pretreatment conditions) compared to Ba carbonates [61]. Similar results were reported by Jeong-Potter et al. [15] for Ru-Na_2O/Al_2O_3 DFM-samples. The authors confirmed that the sample preparation method is inconsequential for Ru DFM systems. Ru in nitrate or oxide form can be sufficiently reduced during in situ prereduction to methanation active Ru^0, thereby catalytically decomposing Na_2CO_3 to ″Na_2O″ and producing more active sites for CO_2 adsorption. Ru indirectly contributes to the enhanced CO_2 adsorption capacity by facilitating the decomposition of the precursor salts, liberating more adsorption sites.

Furthermore, after three cycles of CO_2 adsorption and TPD, the CO_2 uptake of Ba-Ru was found to be completely inhibited (data not shown), resulting in a loss of storage capacity. This inhibition is likely due to the

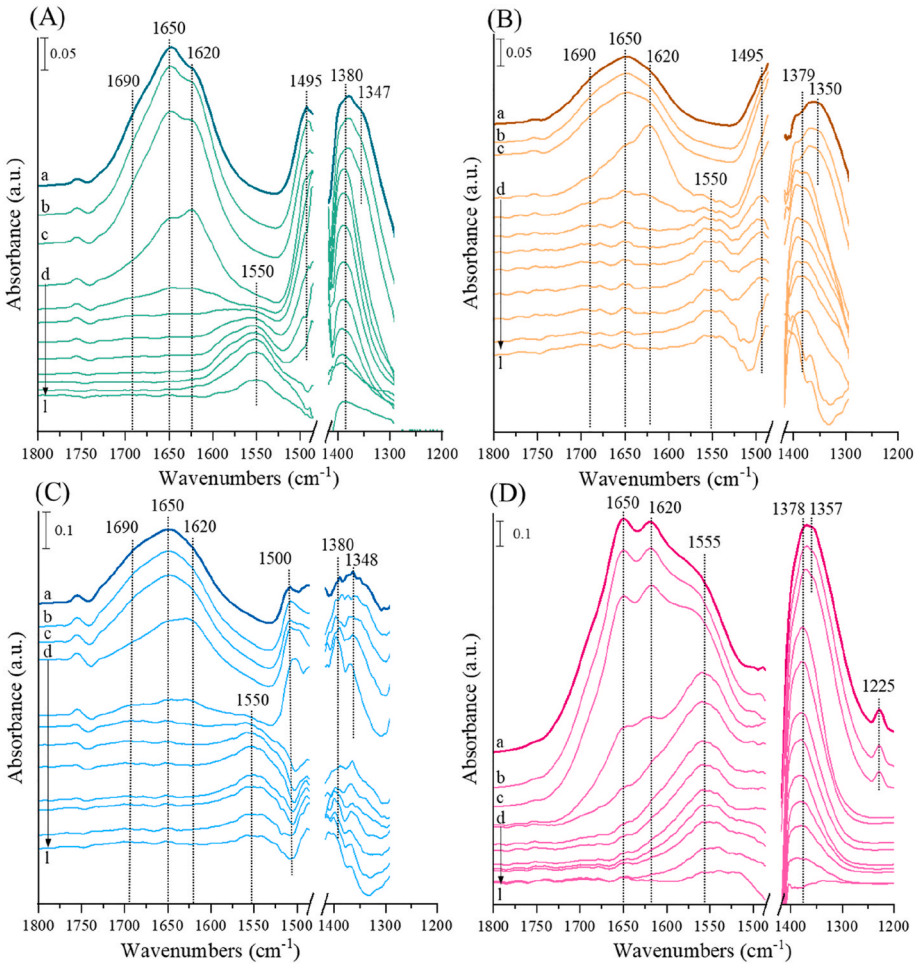

Fig. 9. FT-IR spectra of surface species arising from CO_2 adsorption and desorption over (A) 16Ba-Ru/SiO_2 and (B) Ru-16Ba/SiO_2, (C) Ru-32Ba/SiO_2 and (D) 16Ba-Ru/Al_2O_3 at (a) Presence of 18 Torr CO_2 and (b) 2 Torr CO_2 at R.T. (c) outgassing for 2 min and (d) for 1 h at R.T.; outgassing at increasing temperature in 150 °C to 500 °C (step: 50 °C, curves e-l). The spectrum of the activated surface was subtracted.

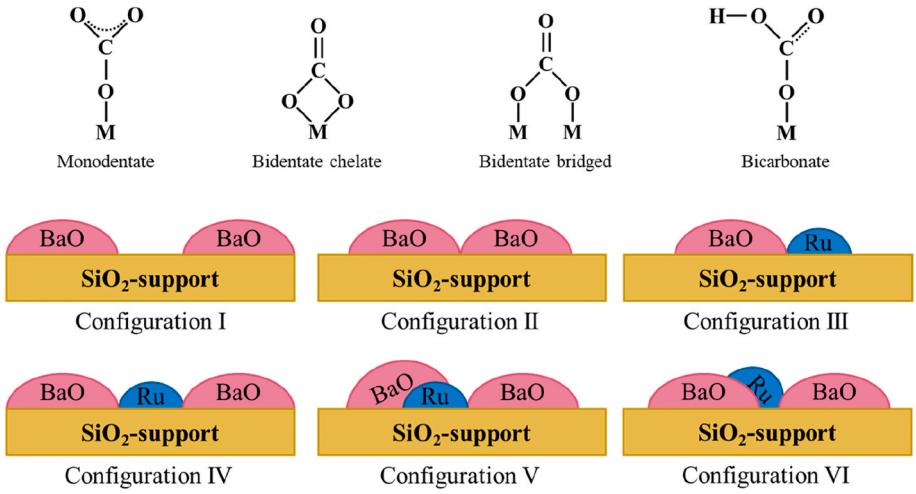

Fig. 10. Schematic representation of different carbonate species (M = Metal) and active phase distributions present over silica support.

increased stability of carbonates in this configuration, caused by the gradual build-up of stable carbonate species. The lower regenerability of Ba-Ru is the main reason for adopting the Ru-Ba impregnation procedure for the preparation of Ru-32Ba/SiO_2.

FT-IR spectra after CO_2 adsorption over Ru-32Ba/SiO_2 catalyst are reported in Fig. 9C. Notably, compared to its analogue with half the Ba concentration (Fig. 9B), the spectral scale is doubled, indicating a higher relative concentration of overall detected species, in line with the overall enhanced CO_2 adsorption capacity (see Table 2). A pronounced formation of monodentate carbonate species, centered at 1347 cm^{-1}, was

observed, that persisted until 150 °C, in contrast to the sample containing 16 wt% Ba. This effect is attributed to a higher surface population of Ba-oxide, which favors the formation of such species. A shoulder at 1690 cm^{-1}, likely corresponding to bicarbonate species on was also detected; these species were rapidly desorbed upon outgassing. Peaks at 1650, 1620, 1500, and 1375 cm^{-1} were attributed to the formation of bidentate chelate carbonates. The weaker bonded species (1650 and 1620 cm^{-1}) disappeared above 150 °C, evolving into bridging bidentate carbonates (1550 cm^{-1}). This bridging carbonate signal remained more thermally stable and exhibited greater intensity compared to the analogous Ru-16Ba/SiO_2 sample. The increased population of isolated and proximal BaO sites appears to favor the formation of strongly adsorbed bridged bidentate carbonates, which gradually desorb, as confirmed by CO_2-TPD tests in a microreactor (Fig. 8c). On the contrary, the formation of bidentate carbonates, associated with BaO in proximity to Ru sites (1500 and 1375 cm^{-1}), was suppressed, consistent with the increased Ba concentration. These species desorbed and became undetectable above 150 °C. Overall, increase the Ba loading results in an improved CO_2 adsorption capacity, mainly achieved through the formation of bidentate chelating carbonates that evolve into bridging bidentate species, considerably more thermally stable (medium-high strength adsorption).

This complex carbonate population could be described considering the superficial distribution of Ba and Ru and their reciprocal proximity; a general scheme is reported in Fig. 10. Chelating bidentate carbonates (1650 and 1620 cm^{-1}) are likely primarily located on isolated or closely spaced barium oxide sites on the catalyst surface (configuration I and II). These species could be weaker bonded than those formed when Ba is close to Ru sites (configuration III). Strongly bonded bidentate chelate species (1495 cm^{-1} band) result from the interaction between Ba and Ru oxide species (configuration IV). Moreover, bidentate chelating carbonates can evolve into bridging bidentate species (1550 cm^{-1}) when they are formed on BaO-BaO centers (configuration II) desorbed gradually at higher temperatures due to stronger bonding carbonate character. When chelating bidentate carbonates species are formed on well-dispersed BaO phase (1495 and 1380 cm^{-1}), a gradually desorption can be observed with temperature, as evidenced by a progressive decrease in their band intensity. Their isolated nature on the catalyst surface prevented their conversion into bridged carbonates.

This FT-IR analysis permits to associate CO_2 desorption peaks observed in during TPD with superficial species of different nature: the stronger bidentate chelated carbonate species desorb progressively with temperature as medium-strength adsorbed species, generating a CO_2 desorption peak at temperature below 250 °C, whereas their evolution into bridging carbonate species (configuration II in Fig. 10), likely occurs only at temperatures higher than 300 °C.

The CO_2 storage capacity of the SiO_2-based catalysts results significantly lower than that of analogous systems based on commercial γ-Al_2O_3 as support [22,25]. In comparison with the silica-supported sample, a larger number of different and strong bands were observed following CO_2 adsorption (Fig. 9D). Indeed, exposed alumina support actively contributes to CO_2 adsorption in the form of surface carbonates and hydrogen carbonates [22,62]. Namely, under CO_2 atmosphere and after outgassing, a diagnostic peak at 1225 cm^{-1}, attributed to the formation of weakly adsorbed bicarbonate species on the alumina support [50,63,64], was observed. These species disappeared after prolonged outgassing. Also bands at 1650 and 1620 cm^{-1}, associated with the formation of bidentate chelated carbonate species, progressively decreased during outgassing at room temperature, disappearing above 200 °C, while a component at 1378 cm^{-1}, again attributed to strongly adsorbed bidentate chelated carbonates, persisted with increasing temperature up to 500 °C band at 1555 cm^{-1} was also observed, becoming the predominant signal after outgassing at increasing temperatures, albeit with a reduction in intensity from 300 °C onward, in parallel with a similar band detected over Silica-based catalysts. This feature could be attributed to the preferential formation of bridging bidentate carbonates likely involving Ba and Ru ionic species.

As a matter of fact, when using this Al_2O_3 as a support, the concentration of Ba and Ru atoms per m^2 is 1.8 times higher than on Silica and this substantially increases the probability of forming highly thermally stable carbonate-type species on close proximity BaO particles, [BaO-BaO]-CO_3. In sum, the thermal stability of predominantly bridged bidentate carbonates (the major population) is higher when alumina is employed; these species require higher temperatures for desorption. On the other side, the use of silica favors the formation of chelated bidentate carbonates, which are less thermally stable and evolve into bridging species that remain adsorbed until higher temperatures are reached.

3.2.2. *Temperature programmed surface reduction with hydrogen (H_2-TPSR)*

As in the case of CO_2-TPD, H_2-TPSR experiments were conducted by combining gas phase analysis from microreactor system with FT-IR spectroscopy. The results of the former are reported in Fig. 11.

On 16Ba-Ru/SiO_2 (Fig. 11A) the adsorbed CO_2 reacts with H_2 to CH_4, that is observed with two maxima at 231 °C and ~420 °C. The CH_4 concentration profile agrees with the presence on the surface of a variety of carbonate species with different stability, as confirmed by the FT-IR CO_2-TPD, and different reactivity towards H_2.

Note that the CH_4 peak is observed in correspondence of that of CO_2 released during TPD. Ru-16Ba/SiO_2 catalyst also results active and selective in the methanation reaction (Fig. 11B), although in this case the methane production is moved at a higher temperature (266 °C). This shift could be likely due to the lower reducibility of these carbonates requiring higher temperature to be converted into methane. In both 16Ba-Ru and Ru-16Ba samples, any other product is observed, neither CO_2 nor CO, suggesting a high selectivity for the methanation reaction on this system. Moreover, considering the amount of CH_4 produced reported in Tables 2 and it is clear that stored CO_2 is not completely converted into methane. In the literature there are indications on the lower performances of SiO_2-based catalysts with respect to other supports (e.g. Al_2O_3, TiO_2, CeO_2), being the apparent activation energies of CO_2 hydrogenation reaction depend on the nature of the support [65]. However, it should be noted that the same selectivity was observed by Porta et al. [22,25,62] on Ru-Ba/Al_2O_3 DFMs. Moreover, these authors observed the release of CO_2 before the methane production while it is absent in our SiO_2-based catalysts. It could be suggested that on Al_2O_3-supported DFMs CO_2 is adsorbed onto the support as well as on the Ba sites, forming more labile bicarbonate species that desorb at low temperature without reaction with H_2. On the other hand, on SiO_2--supported DFMs the acidic nature of the support inhibits the adsorption of CO_2 that occurs preferentially on Ba sites, resulting in more stable carbonates that are reduced to CH_4 at lower temperatures than those on alumina-based material.

When the Ba loading is increased, a CO_2 desorption is still observed at 209 °C (as in the CO_2-TPD) attributed to the cleavage of the weak bicarbonate bands while the CH_4 production starts at slightly higher temperatures, reaching the maximum at 271 °C.

The initial incorporation of the storage element followed by the noble metal promotes a CO_2 capture mechanism that selectively forms a higher population of medium-strength carbonates while maintaining a CO_2 desorption capacity similar to that of the 16Ba-Ru/SiO_2 sample. This effect resulted in a higher overall regeneration capacity at a lower temperature range and with quicker CH_4 generation, with a higher and more symmetric maximum peak. In contrast, when Ru is incorporated after the storage element, a spillover effect is promoted, which is slower and favored at higher temperatures upon H_2 introduction [25,66,67]. However, when the alkali (base) is introduced after Ruthenium in catalysts supported on commercial silica, a portion of Ruthenium becomes blocked by the presence of Ba. This reduces the *spillover* effect, thereby favoring a reduction of the generated carbonates over a wider temperature range, as evidenced by the different CH_4 production temperature ranges in the H_2-TPSR test.

The reducibility of the CO_2 adsorbed species was also investigated by

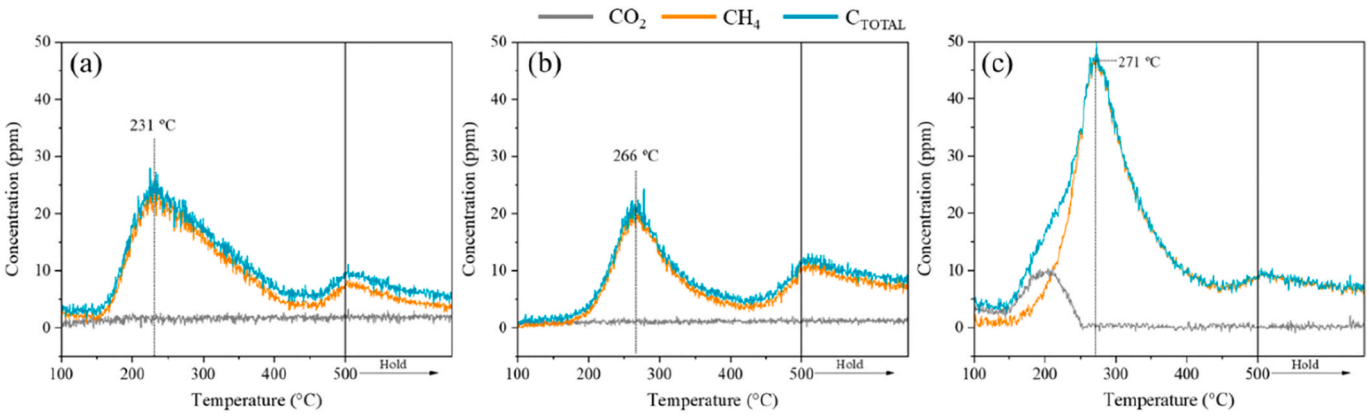

Fig. 11. H_2-TPSR profiles for (a) 16Ba-Ru/SiO_2, (b) Ru-16Ba/SiO_2 and (c) Ru-32Ba/SiO_2.

FT-IR analysis for the 16Ba-Ru/SiO_2 and Ru-16Ba/SiO_2 samples, the results are presented in Fig. 12A and B, respectively. In these experiments, the samples were saturated with CO_2 at room temperature to ensure maximum adsorption and then subjected to prolonged outgassing at room temperature and subsequently to a temperature ramp from 150 °C to 500 °C under a H_2 atmosphere. Note that only carbonates are detected, whose intensity changes under H_2 flow. Potential reaction intermediates, such as Ru-carbonyls or formate species, which have been reported for CO_2 methanation over Ru or Ni based and Na or K based DFM catalysts supported over alumina(-ceria) [30,68–71], could not be clearly identified probably because masked by the more intense carbonate bands and/or by the silica signals in the spectral region of 1200-2050 cm^{-1}.

Consistent with the gas-phase results, a rapid and significant reduction of carbonate species was observed in both samples when hydrogen was introduced as the temperature increased. However, the distribution and evolution of the various carbonate species differed from the FT-IR results recorded during CO_2-TPD (see Fig. 9A–B).

In the case of 16Ba-Ru/SiO_2 sample, a marked reduction in the carbonate signals was observed after introducing H_2 at room temperature and increasing the temperature to 150 °C (Fig. 12A, spectrum b). A complex absorption was detected, with a main maximum at 1624 cm^{-1}, which can be attributed to low-strength bidentate chelated carbonate species as discussed before. Another component centered at 1550 cm^{-1} emerged at increasing temperature. This latter band corresponds to bridging bidentate carbonate species formed via the early conversion of bidentate chelated species to bridging species under reducing conditions at relatively low temperatures. With the increasing temperature to 250 °C, the 1624 cm^{-1} complex band gradually diminished in intensity and then increased again at higher temperature. This behavior suggests that this band could be also associated with vibrational deformation mode of adsorbed water (from the methanation reaction) at the catalyst surface as reported by Kantcheva et al. [55]. A similar trend was observed for the 1550 cm^{-1} band, which slightly increased in intensity above 300 °C. In addition, the bands at 1495 and 1380 cm^{-1}, associated with high-stability bidentate carbonate species, decreased in intensity by rising temperature. Both bidentate chelated and bridging species show significant stability, with the bridging species decomposing and reducing to CH_4 progressively as the temperature increases. Notably, the high-strength bidentate species remain resistant even above 350 °C, gradually diminishing with further temperature rise. It could be supposed that the weakly adsorbed carbonate species, identified as monodentate and bidentate chelated species in the previous section, are rapidly converted to CH_4, while medium-to-high strength carbonates (i.e. bridged bidentate) are likely reduced only at elevated temperatures.

For the Ru-16Ba/SiO_2 sample (Fig. 12B), a slightly different

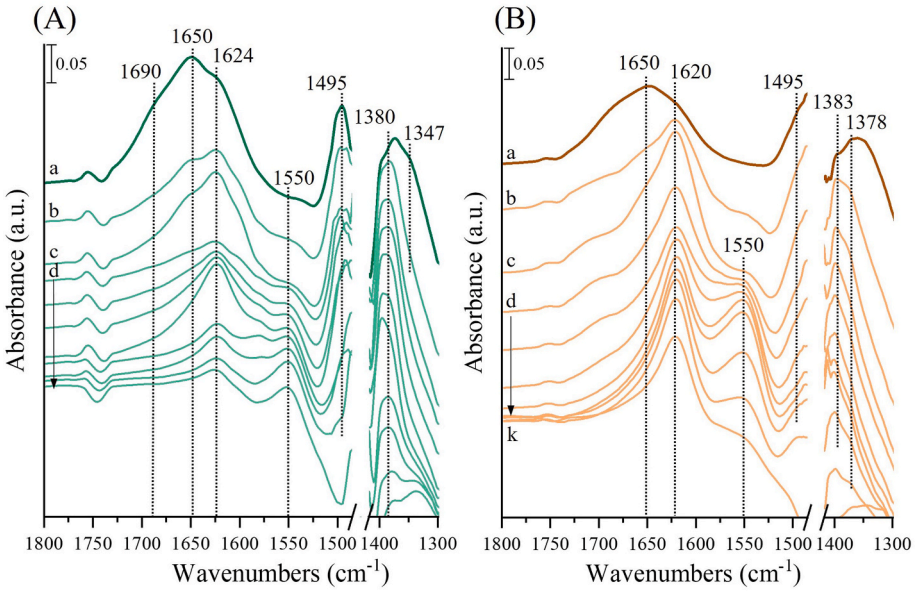

Fig. 12. FT-IR spectra of surface species arising from the H_2-TPSR over (A) 16Ba-Ru/SiO_2 and (B) Ru-16Ba/SiO_2 at (a) Presence of 18 Torr CO_2 at R.T., (b) outgassing 1 h at R.T. in the presence of 150 Torr of H_2 at (c) R.T and (d-k) from 150 to 500 °C by 50 °C/step. The activated spectrum and gas phase spectrum were subtracted.

evolution of adsorbed species was observed. Upon H_2 introduction and increasing the temperature to 150 °C, a significant decrease in intensity was observed in all bands except for the one centered at 1620 cm^{-1}, whose complex assignation is discussed above. From this temperature onward, a distinct peak at 1550 cm^{-1}, attributed to bridging bidentate carbonates, emerged. The sequential incorporation of Ru after Ba (configuration V in Fig. 10) enhanced hydrogen mobility at the Ru active sites via the spillover effect. The good dispersion of basic-adsorption sites and Ru catalytically active sites in high surface and porous support yield to an enhanced DFM performance as Tsiotsias et al. reported [72]. This promoted a more effective transformation of both low-strength (1620 cm^{-1}) and high-strength (1383 cm^{-1}) bidentate chelated carbonates by breaking the coordination bonds at the BaO-BaO centers. Part of the decomposition of these carbonates led to CH_4 formation, as detected in the gas phase spectra (data not shown), while some evolved into bridged species that were progressively reduced to CH_4 with increasing temperature until disappearing at 500 °C. The persistence of the 1620 cm^{-1} band even at 500 °C supports the formation of adsorbed water subsequent to methanation reaction, as discussed before.

4. Concluding remarks

The study investigates the functionalization of silica with basic components and active Ru to create a dual function material for CO_2 methanation reaction, focusing on the effects of Ba loading and impregnation methods. FT-IR and spectroscopic analyses revealed a heterogeneous surface with silanols, basic oxides, and coordinatively unsaturated Lewis sites that promote CO_2 activation.

CO_2 adsorption/desorption studies identified bicarbonate and carbonate species of varying thermal stability, linked to methanation activity. The Ru-16Ba/SiO_2 catalyst favors low-temperature, labile carbonate formation by placing Ru atop Ba, enhancing CO_2 storage and avoiding active phase blockage. Higher Ba loading generates stronger, high-temperature carbonates requiring higher temperature for CH_4 conversion. Surface CO adsorption studies indicate that basic oxides support electron donation to Ru, stabilizing Ru particles under reaction conditions.

The study established a clear relationship between the material's composition and its performance. Furthermore, the sequence in which the components were impregnated proved critical. While the overall CO_2 storage capacity remained largely unaffected at lower Ba concentrations, the preparation order strongly dictated the nature, strength, and regenerability of the adsorbed carbonates. This impregnation sequence also played a key role in positioning the ruthenium methanation catalyst, thereby influencing both the CO_2 conversion activity and the reactivity of the captured carbonate species.

Ultimately, a significant finding was the distinct behavior of SiO_2 support compared to conventional alumina-based systems. The non-interacting nature of the silica support provided an advantage by favoring lower-temperature regeneration, which is beneficial for the overall energy efficiency of the cyclic process. Through detailed structural and surface analyses, the research successfully correlated the formation of specific carbonate populations with the synthesis variables, providing new mechanistic insights. In summary, the work validates mesoporous silica as a viable, tunable, and highly effective support for DFMs, advancing the design of materials tailored for integrated CO_2 capture and methanation technology.

CRediT authorship contribution statement

S. Molina-Ramirez: Writing – original draft, Visualization, Investigation, Formal analysis, Data curation. **G. Nava:** Writing – original draft, Visualization, Investigation, Formal analysis, Data curation. **E. Finocchio:** Writing – review & editing, Writing – original draft, Supervision, Methodology, Conceptualization. **L. Lietti:** Supervision, Conceptualization. **L. Viganò:** Writing – review & editing. **M. Di Virgilio:** Writing – review & editing. **B. Di Credico:** Writing – review & editing. **R. Scotti:** Writing – review & editing. **C. Cristiani:** Writing – review & editing, Project administration, Funding acquisition. **L. Castoldi:** Writing – review & editing, Writing – original draft, Methodology, Conceptualization.

Founding sources

This work has been performed under the financial support of Piano Nazionale di Ripresa e Resilienza funded by the Italian Ministry of University and Research (MUR), in the framework of the European Union - NextGenerationEU - Mission 4 "Education and Research", PRIN 2022 PNRR SILCO-TITOLO (P2022SZANL) Project - CUP: D53D23018550001.

Declaration of competing interest

The authors declare that they have no known competing financial interests or personal relationships that could have appeared to influence the work reported in this paper.

Acknowledgments

Drs. SMR, MDV, and LV are grateful for the financial support of Piano Nazionale di Ripresa e Resilienza funded by the Italian Ministry of University and Research (MUR), in the framework of the European Union - NextGenerationEU - Mission 4 "Education and Research", PRIN 2022 PNRR SILCO-TITOLO (P2022SZANL) Project - CUP: D53D23018550001.

Appendix A. Supplementary data

Supplementary data to this article can be found online at https://doi.org/10.1016/j.micromeso.2026.114080.

Data availability

Data will be made available on request.

References

[1] Rebecca Lindsey, Climate change: atmospheric carbon dioxide, Climate.Gov (NOAA) (2025). https://www.climate.gov/news-features/understanding-climate/climate-change-atmospheric-carbon-dioxide. (Accessed 28 July 2025).

[2] K. Calvin, D. Dasgupta, G. Krinner, A. Mukherji, P.W. Thorne, C. Trisos, J. Romero, P. Aldunce, K. Barrett, G. Blanco, W.W.L. Cheung, S. Connors, F. Denton, A. Diongue-Niang, D. Dodman, M. Garschagen, O. Geden, B. Hayward, C. Jones, F. Jotzo, T. Krug, R. Lasco, Y.-Y. Lee, V. Masson-Delmotte, M. Meinshausen, K. Mintenbeck, A. Mokssit, F.E.L. Otto, M. Pathak, A. Pirani, E. Poloczanska, H.-O. Pörtner, A. Revi, D.C. Roberts, J. Roy, A.C. Ruane, J. Skea, P.R. Shukla, R. Slade, A. Slangen, Y. Sokona, A.A. Sörensson, M. Tignor, D. van Vuuren, Y.-M. Wei, H. Winkler, P. Zhai, Z. Zommers, J.-C. Hourcade, F.X. Johnson, S. Pachauri, N. P. Simpson, C. Singh, A. Thomas, E. Totin, A. Alegría, K. Armour, B. Bednar-Friedl, K. Blok, G. Cissé, F. Dentener, S. Eriksen, E. Fischer, G. Garner, C. Guivarch, M. Haasnoot, G. Hansen, M. Hauser, E. Hawkins, T. Hermans, R. Kopp, N. Leprince-Ringuet, J. Lewis, D. Ley, C. Ludden, L. Niamir, Z. Nicholls, S. Some, S. Szopa, B. Trewin, K.-I. van der Wijst, G. Winter, M. Witting, A. Birt, M. Ha, IPCC, Climate change 2023: synthesis report, in: H. Lee, J. Romero (Eds.), Contribution of Working Groups I, II and III to the Sixth Assessment Report of the Intergovernmental Panel on Climate Change [Core Writing Team, IPCC, Geneva, Switzerland, 2023, https://doi.org/10.59327/IPCC/AR6-9789291691647, 2023.

[3] P.A. Saenz Cavazos, E. Hunter-Sellars, P. Iacomi, S.R. McIntyre, D. Danaci, D. R. Williams, Evaluating solid sorbents for CO2 capture: linking material properties and process efficiency via adsorption performance, Front. Energy Res. 11 (2023), https://doi.org/10.3389/fenrg.2023.1167043.

[4] H. Zentou, B. Hoque, M.A. Abdalla, A.F. Saber, O.Y. Abdelaziz, M. Aliyu, A. M. Alkhedhair, A.J. Alabduly, M.M. Abdelnaby, Recent advances and challenges in solid sorbents for CO2 capture, Carbon Capture Sci. Technol. 15 (2025) 100386, https://doi.org/10.1016/j.ccst.2025.100386.

[5] NOAA Research, No sign of greenhouse gases increases slowing in 2023. https://research.noaa.gov/no-sign-of-greenhouse-gases-increases-slowing-in-2023/, 2024. (Accessed 28 July 2025).

[6] Y. Wang, L. Zhao, A. Otto, M. Robinius, D. Stolten, A review of post-combustion CO2 capture technologies from coal-fired power plants, Energy Proc. 114 (2017) 650–665, https://doi.org/10.1016/j.egypro.2017.03.1209.

[7] F. Raganati, F. Miccio, P. Ammendola, Adsorption of carbon dioxide for post-combustion capture: a review, Energy Fuel. 35 (2021) 12845–12868, https://doi.org/10.1021/acs.energyfuels.1c01618.

[8] S. Molina-Ramírez, D. Peltzer, M. Cortés-Reyes, C. Herrera, M.A. Larrubia, L. Cornaglia, L.J. Alemany, CO2-SR technology using NiBa unsupported catalyst. Isotopic study of cyclic process of CO2 storage and in situ regeneration with CH4, Fuel 341 (2023) 127690, https://doi.org/10.1016/j.fuel.2023.127690.

[9] A. Porta, C. Larghi, L. Lietti, C.G. Visconti, Once-through CO2 hydrogenation to grid-compatible synthetic natural gas over a Ru-based catalyst at atmospheric pressure, Catal. Today 442 (2024) 114907, https://doi.org/10.1016/j.cattod.2024.114907.

[10] P. Frontera, A. Macario, M. Ferraro, P.L. Antonucci, Supported catalysts for CO2 methanation: a review, Catalysts 7 (2017), https://doi.org/10.3390/catal7020059.

[11] C. Shen, M. Liu, S. He, H. Zhao, C. Liu, Advances in the studies of the supported ruthenium catalysts for CO2 methanation, Chin. J. Catal. 63 (2024) 1–15, https://doi.org/10.1016/S1872-2067(24)60090-2.

[12] A.B. Rao, E.S. Rubin, A technical, economic, and environmental assessment of amine-based CO $_2$ capture technology for power plant greenhouse gas control, Environ. Sci. Technol. 36 (2002) 4467–4475, https://doi.org/10.1021/es0158861.

[13] M.S. Duyar, M.A.A. Treviño, R.J. Farrauto, Dual function materials for CO 2 capture and conversion using renewable H 2, Appl. Catal., B 168–169 (2015) 370–376, https://doi.org/10.1016/j.apcatb.2014.12.025.

[14] R.J.; D.M.S., P.A.A. Farrauto, Methods, Systems, and Materials for Capturing Carbon Dioxide and Converting it to a Chemical Product, 2016. WO2016/007825A1.

[15] C. Jeong-Potter, M. Abdallah, S. Kota, R. Farrauto, Enhancing the CO $_2$ adsorption capacity of γ-Al $_2$ O $_3$ supported alkali and alkaline-earth metals: impacts of dual function material (DFM) preparation methods, Ind. Eng. Chem. Res. 61 (2022) 10474–10482, https://doi.org/10.1021/acs.iecr.2c00364.

[16] A. Porta, C.G. Visconti, L. Castoldi, R. Matarrese, C. Jeong-Potter, R. Farrauto, L. Lietti, Ru-Ba synergistic effect in dual functioning materials for cyclic CO2 capture and methanation, Appl. Catal., B 283 (2021) 119654, https://doi.org/10.1016/J.APCATB.2020.119654.

[17] G. Nava, A. Porta, C.G. Visconti, R. Matarrese, Impact of sorbent-catalyst layouts on Ru/K-based DFMs for integrated CO2 capture and methanation, Appl. Catal. Gen. 709 (2026) 120654, https://doi.org/10.1016/j.apcata.2025.120654.

[18] M.A. Arellano-Treviño, Z. He, M.C. Libby, R.J. Farrauto, Catalysts and adsorbents for CO2 capture and conversion with dual function materials: limitations of Ni-containing DFMs for flue gas applications, J. CO2 Util. 31 (2019) 143–151, https://doi.org/10.1016/j.jcou.2019.03.009.

[19] C. Jeong-Potter, A. Porta, R. Matarrese, C.G. Visconti, L. Lietti, R. Farrauto, Aging study of low Ru loading dual function materials (DFM) for combined power plant effluent CO2 capture and methanation, Appl. Catal., B 310 (2022) 121294, https://doi.org/10.1016/j.apcatb.2022.121294.

[20] A. Bermejo-López, B. Pereda-Ayo, J.A. Onrubia-Calvo, J.A. González-Marcos, J. R. González-Velasco, Aging studies on dual function materials Ru/Ni-Na/Ca-Al2O3 for CO2 adsorption and hydrogenation to CH4, J. Environ. Chem. Eng. 10 (2022) 107951, https://doi.org/10.1016/j.jece.2022.107951.

[21] S. Cimino, F. Boccia, L. Lisi, Effect of alkali promoters (Li, Na, K) on the performance of Ru/Al2O3 catalysts for CO2 capture and hydrogenation to methane, J. CO2 Util. 37 (2020) 195–203, https://doi.org/10.1016/j.jcou.2019.12.010.

[22] A. Porta, R. Matarrese, C.G. Visconti, L. Castoldi, L. Lietti, Storage material effects on the performance of Ru-Based CO $_2$ capture and methanation dual functioning materials, Ind. Eng. Chem. Res. 60 (2021) 6706–6718, https://doi.org/10.1021/acs.iecr.0c05898.

[23] M.S. Duyar, S. Wang, M.A. Arellano-Treviño, R.J. Farrauto, CO 2 utilization with a novel dual function material (DFM) for capture and catalytic conversion to synthetic natural gas: an update, J. CO2 Util. 15 (2016) 65–71, https://doi.org/10.1016/j.jcou.2016.05.003.

[24] S. Essounani-Mérida, S. Molina-Ramírez, M. Cortés-Reyes, C. Herrera, M.Á. Larrubia, L.J. Alemany, Influence of second metal incorporation on nickel-based unsupported catalysts for CO2 reduction (CO2-SR) technology, Results Eng. 26 (2025) 104921, https://doi.org/10.1016/j.rineng.2025.104921.

[25] A. Porta, C.G. Visconti, L. Castoldi, R. Matarrese, C. Jeong-Potter, R. Farrauto, L. Lietti, Ru-Ba synergistic effect in dual functioning materials for cyclic CO2 capture and methanation, Appl. Catal., B 283 (2021) 119654, https://doi.org/10.1016/j.apcatb.2020.119654.

[26] A. Bermejo-López, B. Pereda-Ayo, J.A. Onrubia-Calvo, J.A. González-Marcos, J. R. González-Velasco, How the presence of O2 and NOx influences the alternate cycles of CO2 adsorption and hydrogenation to CH4 on Ru-Na-Ca/Al2O3 dual function material, J. CO2 Util. 67 (2023) 102343, https://doi.org/10.1016/j.jcou.2022.102343.

[27] J.A. Onrubia-Calvo, A. Bermejo-López, S. Pérez-Vázquez, B. Pereda-Ayo, J. A. González-Marcos, J.R. González-Velasco, Applicability of LaNiO3-derived catalysts as dual function materials for CO2 capture and in-situ conversion to methane, Fuel 320 (2022) 123842, https://doi.org/10.1016/J.FUEL.2022.123842.

[28] J.A. Onrubia-Calvo, B. Pereda-Ayo, J.A. González-Marcos, J.R. González-Velasco, Lanthanum partial substitution by basic cations in LaNiO3/CeO2 precursors to raise DFM performance for integrated CO2 capture and methanation, J. CO2 Util. 81 (2024) 102704, https://doi.org/10.1016/J.JCOU.2024.102704.

[29] E. Bracciotti, D. Salusso, I. López-Luque, S. Bertinetti, L.A. Luque-Álvarez, L. F. Bobadilla, G. Prieto, M. Moliner, S. Bordiga, S. Rojas-Buzo, Structural and electronic modulation by Ce-doping in MOF-derived In2O3@CeO2-ZrO2 catalysts for CO2 hydrogenation, Chem. Eng. J. 527 (2026) 171706, https://doi.org/10.1016/j.cej.2025.171706.

[30] L.-P. Merkouri, J.L. Martín-Espejo, L.F. Bobadilla, J.A. Odriozola, M.S. Duyar, T. R. Reina, Flexible NiRu systems for CO2 methanation: from efficient catalysts to advanced dual-function materials, Nanomaterials 13 (2023) 506, https://doi.org/10.3390/nano13030506.

[31] S. Bahrami Gharamaleki, S. Carrasco Ruiz, T. Ramirez Reina, M. Short, M.S. Duyar, Effect of adsorbent loading on NaNiRu-DFMs' CO $_2$ capture and methanation: finding optimal Na-loading using Bayesian optimisation guided experiments, Industrial Chemistry & Materials (2026), https://doi.org/10.1039/D5IM00019J.

[32] S. Cimino, E.M. Cepollaro, L. Lisi, On the effect of Li or Na doping on Ru/TiO2 catalyst for CO2 methanation, Catal. Today 452 (2025) 115245, https://doi.org/10.1016/j.cattod.2025.115245.

[33] W. Zhang, H. Lin, Y. Wei, X. Zhou, Y. An, Y. Dai, Q. Niu, T. Lin, L. Zhong, Overturning CO $_2$ hydrogenation selectivity via strong metal–support interaction, ACS Catal. 14 (2024) 2409–2417, https://doi.org/10.1021/acscatal.3c05527.

[34] Y. Li, Z. Liu, Z. Rao, F. Yu, W. Bao, Y. Tang, H. Zhao, J. Zhang, Z. Wang, J. Li, Z. Huang, Y. Zhou, Y. Li, B. Dai, Experimental and theoretical insights into an enhanced CO2 methanation mechanism over a Ru-based catalyst, Appl. Catal., B 319 (2022) 121903, https://doi.org/10.1016/j.apcatb.2022.121903.

[35] J. Ilsemann, M.M. Murshed, T.M. Gesing, J. Kopyscinski, M. Bäumer, On the support dependency of the CO $_2$ methanation – decoupling size and support effects, Catal. Sci. Technol. 11 (2021) 4098–4114, https://doi.org/10.1039/D1CY00399B.

[36] M. Mihet, M. Dan, L. Barbu-Tudoran, M.D. Lazar, CO2 methanation using multimodal Ni/SiO2 catalysts: effect of support modification by MgO, CeO2, and La2O3, Catalysts 11 (2021) 443, https://doi.org/10.3390/catal11040443.

[37] A.A.A. Mohammed, P. Ebrahimi, A. Yuda, M.J. Al-Marri, A. Kumar, M. Ali, H. S. Saad, Role of Ca in Ni-Ca/Fumed-SiO2 catalysts for CO2 catalytic conversion to methane, Top. Catal. 68 (2025) 1003–1016, https://doi.org/10.1007/s11244-024-02010-x.

[38] G. Bergeret, P. Gallezot, Particle size and dispersion measurements, in: Handbook of Heterogeneous Catalysis, Wiley, 2008, pp. 738–765, https://doi.org/10.1002/9783527610044.hetcat0038.

[39] L.M. Bravo, F.C. Meunier, J. Kopyscinski, Rare earth oxide promoted Ru/Al2O3 dual function materials for CO2 capture and methanation: an operando DRIFTS and TGA study, Appl. Catal. B Environ. Energy 361 (2025) 124591, https://doi.org/10.1016/j.apcatb.2024.124591.

[40] M. Thommes, K. Kaneko, A.V. Neimark, J.P. Olivier, F. Rodriguez-Reinoso, J. Rouquerol, K.S.W. Sing, Physisorption of gases, with special reference to the evaluation of surface area and pore size distribution (IUPAC technical report), Pure Appl. Chem. 87 (2015) 1051–1069, https://doi.org/10.1515/pac-2014-1117.

[41] T. Oliveira Cabral, F. Bellot Noronha, F. Souza Toniolo, Kinetic and DRIFTS studies of the CO2 catalytic hydrogenation on Ru/SiO2: a comprehensive and strategic investigation of CO2 methanation mechanisms by kinetic modeling and data regression, Chem. Eng. J. 485 (2024) 149716, https://doi.org/10.1016/j.cej.2024.149716.

[42] A. Infantes-Molina, L. Righini, L. Castoldi, C.V. Loricera, J.L.G. Fierro, A. Sin, L. Lietti, Characterization and reactivity of Ce-promoted PtBa lean NOx trap catalysts, Catal. Today 197 (2012) 178–189, https://doi.org/10.1016/j.cattod.2012.07.036.

[43] G. Busca, Infrared (IR) spectroscopy, in: Springer Handbook of Advanced Catalyst Characterization, 2023, pp. 3–32, https://doi.org/10.1007/978-3-031-07125-6_1.

[44] L.M.F. Lopes, L.M. Ilharco, Hydrofluoric acid-induced fluorination and formation of silica nanocapsules for ^{19} F magnetic resonance imaging, RSC Adv. 4 (2014) 16931–16934, https://doi.org/10.1039/C3RA47842D.

[45] G. Busca, V. Lorenzelli, Infrared spectroscopic identification of species arising from reactive adsorption of carbon oxides on metal oxide surfaces, Mater. Chem. 7 (1982) 89–126, https://doi.org/10.1016/0390-6035(82)90059-1.

[46] G. Ramis, G. Busca, V. Lorenzelli, Low-temperature CO2 adsorption on metal oxides: spectroscopic characterization of some weakly adsorbed species, Mater. Chem. Phys. 29 (1991) 425–435, https://doi.org/10.1016/0254-0584(91)90037-U.

[47] G. Busca, Catalytic materials based on silica and alumina: structural features and generation of surface acidity, Prog. Mater. Sci. 104 (2019) 215–249, https://doi.org/10.1016/j.pmatsci.2019.04.003.

[48] G. Busca, Spectroscopic characterization of the acid properties of metal oxide catalysts, Catal. Today 41 (1998) 191–206, https://doi.org/10.1016/S0920-5861(98)00049-2.

[49] G. Busca, The surface acidity of solid oxides and its characterization by IR spectroscopic methods. An attempt at systematization, Phys. Chem. Chem. Phys. 1 (1999) 723–736, https://doi.org/10.1039/a808366e.

[50] G. Garbarino, D. Bellotti, E. Finocchio, L. Magistri, G. Busca, Methanation of carbon dioxide on Ru/Al2O3: catalytic activity and infrared study, Catal. Today 277 (2016) 21–28, https://doi.org/10.1016/j.cattod.2015.12.010.

[51] P.A. Kots, T. Xie, B.C. Vance, C.M. Quinn, M.D. de Mello, J.A. Boscoboinik, C. Wang, P. Kumar, E.A. Stach, N.S. Marinkovic, L. Ma, S.N. Ehrlich, D.G. Vlachos, Electronic modulation of metal-support interactions improves polypropylene hydrogenolysis over ruthenium catalysts, Nat. Commun. 13 (2022) 5186, https://doi.org/10.1038/s41467-022-32934-5.

[52] K.I. Hadjiivanov, G.N. Vayssilov, in: Characterization of Oxide Surfaces and Zeolites by Carbon Monoxide as an IR Probe Molecule, 2002, pp. 307–511, https://doi.org/10.1016/S0360-0564(02)47008-3.

[53] S.Y. Chin, C.T. Williams, M.D. Amiridis, FTIR studies of CO adsorption on Al $_2$ O $_3$ - and SiO $_2$ -Supported Ru catalysts, J. Phys. Chem. B 110 (2006) 871–882, https://doi.org/10.1021/jp053908q.

[54] R.A. Dalla Betta, Carbon monoxide adsorption on supported ruthenium, J. Phys. Chem. 79 (1975) 2519–2525, https://doi.org/10.1021/j100590a015.
[55] M. Kantcheva, S. Sayan, On the mechanism of CO adsorption on a silica-supported ruthenium catalyst, Catal. Lett. 60 (1999) 27–38, https://doi.org/10.1023/A:1019082218590.
[56] K. Hadjiivanov, J.-C. Lavalley, J. Lamotte, F. Maugé, J. Saint-Just, M. Che, FTIR study of CO interaction with Ru/TiO2Catalysts, J. Catal. 176 (1998) 415–425, https://doi.org/10.1006/jcat.1998.2038.
[57] F. Frola, F. Prinetto, G. Ghiotti, L. Castoldi, I. Nova, L. Lietti, P. Forzatti, Combined in situ FT-IR and TRM analysis of the NOx storage properties of Pt-Ba/Al2O3 LNT catalysts, Catal. Today 126 (2007) 81–89, https://doi.org/10.1016/j.cattod.2006.10.010.
[58] F. Prinetto, M. Manzoli, S. Morandi, F. Frola, G. Ghiotti, L. Castoldi, L. Lietti, P. Forzatti, Pt−K/Al $_2$ O $_3$ NSR catalysts: characterization of morphological, structural and surface properties, J. Phys. Chem. C 114 (2010) 1127–1138, https://doi.org/10.1021/jp909026p.
[59] F. Frola, M. Manzoli, F. Prinetto, G. Ghiotti, L. Castoldi, L. Lietti, Pt−Ba/Al $_2$ O $_3$ NSR catalysts at different Ba loading: characterization of morphological, structural, and surface properties, J. Phys. Chem. C 112 (2008) 12869–12878, https://doi.org/10.1021/jp801480t.
[60] L. Castoldi, L. Lietti, I. Nova, R. Matarrese, P. Forzatti, F. Vindigni, S. Morandi, F. Prinetto, G. Ghiotti, Alkaline- and alkaline-earth oxides based lean NOx traps: effect of the storage component on the catalytic reactivity, Chem. Eng. J. 161 (2010) 416–423, https://doi.org/10.1016/j.cej.2009.10.065.
[61] A. Porta, R. Matarrese, C.G. Visconti, L. Lietti, Spatially resolved insights from operando FT-IR on integrated CO2 capture and hydrogenation in the presence of NOx, Chem. Eng. J. 521 (2025) 166577, https://doi.org/10.1016/j.cej.2025.166577.
[62] A. Porta, R. Matarrese, C.G. Visconti, L. Lietti, Investigation of DFMs for CO $_2$ capture and methanation by coupled microreactor experiments and FT-IR spectroscopy, Energy Fuel. 37 (2023) 7280–7290, https://doi.org/10.1021/acs.energyfuels.3c00443.
[63] T. Montanari, L. Castoldi, L. Lietti, G. Busca, Basic catalysis and catalysis assisted by basicity: FT-IR and TPD characterization of potassium-doped alumina, Appl. Catal. Gen. 400 (2011) 61–69, https://doi.org/10.1016/j.apcata.2011.04.016.
[64] I. Malpartida, M. Vargas, L. Alemany, E. Finocchio, G. Busca, Pt–Ba–Al2O3 for NOx storage and reduction: characterization of the dispersed species, Appl. Catal., B 80 (2008) 214–225, https://doi.org/10.1016/j.apcatb.2007.11.035.
[65] P. Panagiotopoulou, D.I. Kondarides, XenophonE. Verykios, Selective methanation of CO over supported Ru catalysts, Appl. Catal., B 88 (2009) 470–478, https://doi.org/10.1016/j.apcatb.2008.10.012.
[66] C.-H. Yeh, H.V. Thang, Y.I.A. Reyes, C. Coluccini, H.-Y.T. Chen, DFT insights into hydrogen spillover mechanisms: effects of metal species, size, and support, J. Phys. Chem. C 129 (2025) 6185–6195, https://doi.org/10.1021/acs.jpcc.4c08097.
[67] A. Misol, I. Giarnieri, F. Ospitali, A. Ballarini, J. Jiménez-Jiménez, E. Rodríguez-Castellón, F.M. Labajos, G. Fornasari, P. Benito, CO2 hydrogenation over Ru hydrotalcite-derived catalysts, Catal. Today 425 (2024) 114362, https://doi.org/10.1016/j.cattod.2023.114362.
[68] X. Wang, Y. Hong, H. Shi, J. Szanyi, Kinetic modeling and transient DRIFTS–MS studies of CO2 methanation over Ru/Al2O3 catalysts, J. Catal. 343 (2016) 185–195, https://doi.org/10.1016/j.jcat.2016.02.001.
[69] L. Proaño, E. Tello, M.A. Arellano-Trevino, S. Wang, R.J. Farrauto, M. Cobo, In-situ DRIFTS study of two-step CO2 capture and catalytic methanation over Ru,"Na2O"/Al2O3 dual functional material, Appl. Surf. Sci. 479 (2019) 25–30, https://doi.org/10.1016/j.apsusc.2019.01.281.
[70] L. Falbo, C.G. Visconti, L. Lietti, J. Szanyi, The effect of CO on CO2 methanation over Ru/Al2O3 catalysts: a combined steady-state reactivity and transient DRIFT spectroscopy study, Appl. Catal., B 256 (2019) 117791, https://doi.org/10.1016/j.apcatb.2019.117791.
[71] L. Proaño, M.A. Arellano-Treviño, R.J. Farrauto, M. Figueredo, C. Jeong-Potter, M. Cobo, Mechanistic assessment of dual function materials, composed of Ru-Ni, Na2O/Al2O3 and Pt-Ni, Na2O/Al2O3, for CO2 capture and methanation by in-situ DRIFTS, Appl. Surf. Sci. 533 (2020) 147469, https://doi.org/10.1016/j.apsusc.2020.147469.
[72] A.I. Tsiotsias, N.D. Charisiou, A.G.S. Hussien, A.A. Dabbawala, V. Sebastian, K. Polychronopoulou, M.A. Goula, CO2 capture and methanation using Ru/Na2O/Al2O3 dual-function materials: effect of support synthesis method and Ru load, J. Environ. Chem. Eng. 12 (2024) 112712, https://doi.org/10.1016/j.jece.2024.112712.